博士論文（要約）

「Study on Mechanism of Vortex Breakdown from Aspects of Topology and Stability （トポロジー及び安定性の観点からの渦崩壊現象のメカニズムに関する研究）」

山田　健翔

Contents

List of Figures

List of Tables

Chapter 1

Introduction

Vortex breakdown is still a big ocean of new research findings since its occurrence over a delta wing was found in 1950's [46]. It is a drastical change in a longitudinal vortex and is observed in various situations where the longitudinal vortex exists. It is known that the vortex breakdown takes place in a very wide range from a flow in a small pipe [29] even to a flow in a tornado [51].

On one side, this phenomenon is undesired to take place. It causes a loss in lift and an increase in a pitching-up moment for a case of an aircraft with the delta wing [28] and it causes a rotating stall for a case of a turbine blade [23]. Then, the aim of studies on the vortex breakdown at this side is how it is vanished or weakened.

On the other side, this phenomenon is desired to take place. As the vortex breakdown yields a recirculating region and a strong shear flow, it can be exploited to a device of mixing enhancement such as a swirl burner [60]. These days, it is also applied to a bioreactor to efficiently feeding a cell [62]. Then, the aim of studies on the vortex breakdown at this side is how it is generated and kept.

By means of the both sides, it is very important and expected to reveal the physical property of the vortex breakdown which will lead to let this phenomenon under control. In this thesis, we investigate fundamental properties of the vortex breakdown. Then, this chapter gives what is the fundamental properties, what has been understood so far, and what sholud be investigated at the present state.

The fundamental research of the vortex breakdown is mainly classified to two ways, streamline topology and stability. It is because they are keys to classify the vortex breakdown to several types. Before reviewing previous studies on the fundamental properties of the vortex breakdown, we need to explain the classification of the vortex breakdown. There are roughly two types of the vortex breakdown coming from the observation of particle traces in experiments [54].

One is called *bubble-type*, because the particle traces seem to create a bubble. Its nature is a recirculating flow region yielded along the axis of the longitudinal vortex as shown in Fig. 1.1. It

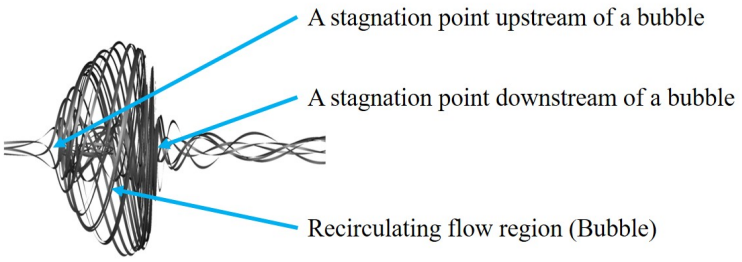

Figure 1.1: Streamlines of bubble-type vortex breakdown

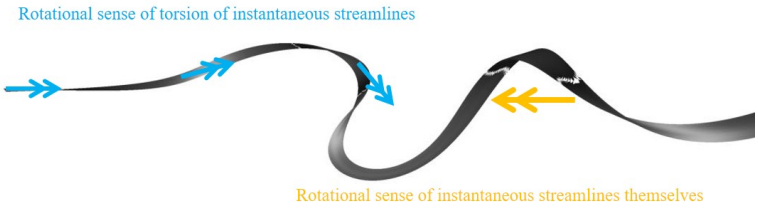

Figure 1.2: Instantaneous streamlines of spiral-type vortex breakdown

means the topological structure of streamlines changes when the bubble-type vortex breakdown takes place. When a tracer particle is trapped into the recirculating flow region, it seems that the bubble is created. Then, the streamline topology is the most important property of the onset of the bubble-type vortex breakdown.

The other is called *spiral-type*, because the particle traces are swirling. It is essencially an unsteady flow. The particle trace (or an intantaneous streamline) is rotating and its rotating sense is opposite to that of the longitudinal vortex. Fig. 1.2 schematically shows this relation using the instantaneous streamlines. It is often said that the spiral-type vortex breakdown follows the buble-type vortex breakdown as a perodic emission of Kármán vortices follows a pair of twin vortices at a wake of a cylinder [14]. The transition from the twin vortices to the Kármán vortices is explained by a flow stability consisting of a growth rate and a frequency in time [70]. Then, the flow stability is the most important property of the transition from the bubble-type to the spiral-type.

Fig. 1.3 shows a relation between the bubble-type vortex breakdown and two properties: the streamline topology and the stability. These two properties are investigated in this thesis. Below, we review the previous studies and describe what is specifically investigated in this thesis. Before that, we introduce dynamical system theory which is common to both analyses. A dynamical system is defined as a set of differential equations evolving in time. The dynamical system theory

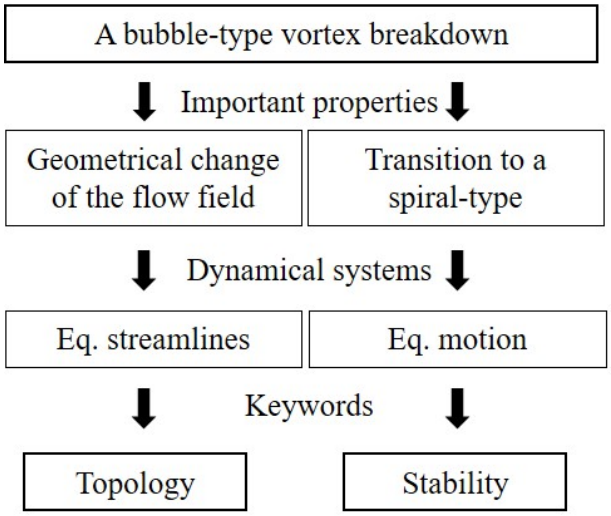

Figure 1.3: Schematical relation between bubble-type vortex breakdown and two properties: streamline topology and stability

treats how many possible patterns there are about topological changes, called *bifurcation*, in solutions of the system and how stable the solutions are (if they are not stable, they are not observed in real). The difference between them is in governing equations. The streamline topology is about a dynamical system of equations of streamlines, and the stability is about a dynamical system of equations of motion. In this thesis, both properties are investigated based on seveal theories. They are explained in detail at Chapter 2.

1.1 Streamline topology of bubble-type vortex breakdown

Studies on topologies of flow fields mean to understand topological structure of integral curves. In the flow fields, there are three types of the integral curves. One is a streamline, which is an integral curve of the velocity vector field frozen in time. Taking a snapshot of the flow field and integrating a line along the velocity vector, we can see the streamline. Second is a streakline, which consists of positions of particles which pass a chosen point. We can see the streakline even in our daily life: smoke is a typical example. Third is a pathline, which is a trajectory a particle follows. If we record the position of the particle in time, we can see the pathline by conneting the positions. We can see the pathline in a stroboscopic picture when we throw a ball and trace its position, for example.

These three lines coincide for a steady flow. When we consider to analyze the topological

structure of those lines, we look for *limit sets* such as a stagnation point, an attracting line, a repelling line, and so on, because we can understand the topology of the flow as a dynamical system. The dynamical system of streamlines enables us to simplify complicated structure of the flow and it was often applied to understand separated flows. Lots of results are summarized in review papers by Tobak and Peake [63], and Perry and Chong [47].

1.1.1 Streamline topology of linear dynamical system

The classification of flow patterns around a stagnation point in a three-dimensional flow field was completed by Chong *et al.* [15]. We review how to classify the flow around the stagnation point. System of equations are simply written as

$$\frac{d}{dt}\mathbf{x} = \mathbf{u}(\mathbf{x}), \tag{1.1}$$

where $\mathbf{x}$ is a position vector and $\mathbf{u}$ is a velocity vector which is a function of $\mathbf{x}$. Consider a stagnation point is found. Linearizing Eq. 1.1 at the stagnation point, we obtain a system of linear equations writen as

$$\frac{d}{dt}\mathbf{x} = A(\mathbf{x} - \mathbf{x}_0), \tag{1.2}$$

where $\mathbf{x}_0$ is the position vector of the stagnation point and A is a matrix called *velocity gradient tensor* defined as

$$A = \partial_{\mathbf{x}}\mathbf{u}(\mathbf{x}_0). \tag{1.3}$$

The velocity gradient tensor has eigenvalues and eigenvectors. These eigenproperties tell us how the flow pattern is. In a two-dimensional flow field, for example, the flow patterns count 5. Those patterns are shown in Fig. 1.4. Based on this analysis, the topological structure of a localized flow around the stagnation point can be determined.

A problem of this analysis is, however, we can understand only the localized flow around the stagnation point. We often see streamlines with plural stagnation points. The dynamical system including these streamlines is no longer a linear system, because the linear system never has plural stagnation points. Then, another method was required to solve this problem.

1.1.2 Streamline topology of nonlinear dynamical system

The local bifurcation theory of fixed points treats the topological change or the bifurcation of a vector field with fixed points. The fixed point is a point where the velocity vector is zero in a space. Then, a stagnation point is always one of the fixed points. By this theory, we can explain a case where a vector field with a single fixed point bifurcates to that with a few fixed points. An important key is to consider the simplest nonlinearity of the dynamical system. This theory was

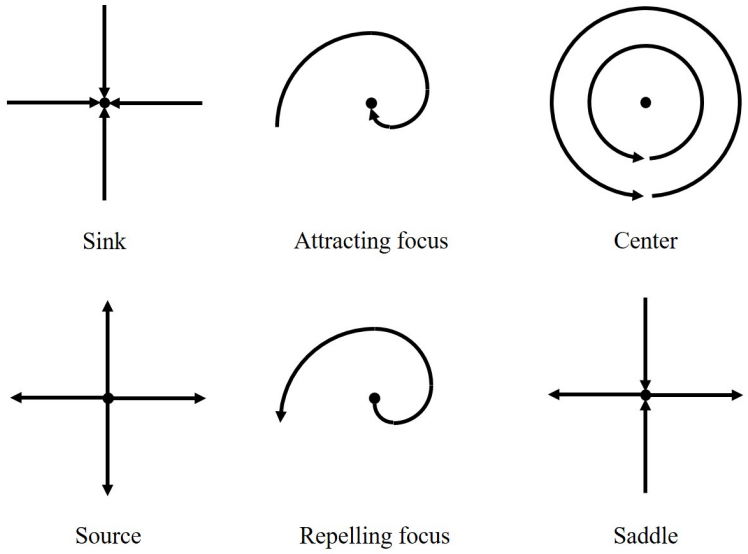

Figure 1.4: Flow patterns around stagnation points in two-dimensional flow fields

developed and explained in detail by Guckenheimer and Holmes [27]. It is explained in Chapter 2. The local bifurcation theory was applied to the analysis on topologies of a wake of a cylinder [17], a two-dimensional separated flow [10]. Possible patterns of the topologies were revealed.

Chaos is one of big themes in the context of dynamical systems. Beggining from the Lorenz attractor [39], it has been revealed that dynamical systems can deterministically be unpredictable. The chaotic bifurcation can take place on a nonlinear dynamical system by perturbations In order to know whether the chaos appears or not, we often see there exists a random region in a Poincaré section [20].

1.1.3 Previous studies on bubble-type vortex breakdown

Above topological analyses were also applied to vortex breakdowns. The reason why researchers analyze a flow topology of a bubble-type vortex breakdown is to determine the topology observed in real and to investigate whether other patterns of the topology possibly exist or not. Some of previous studies are extracted and summarized in Table 1.1.

The eigenvalue analysis of a velocity gradient tensor at a stagnation point was applied to a bubble-type vortex breakdown [66]. It revealed that a pair of stagnation points bounding a recirculating flow region have the structure of a saddle-focus. The difference bitween them is whether the focus is attracting or not. One is a repelling focus, and the other is an attracting focus as shown in Fig. 1.5.

Table 1.1: Review of topological analysis on vortex breakdown

Year	Group	Contents
1994	Blackmore [8]	Polynomial expression of bubble satisfying axisymmetric NS
1995	Visbal [66]	Eigenanaysis of velocity gradient tensor at stagnation points
1999	Brøns *et al.* [13]	Bifurcation model of an axisymmetric incompressible bubble on the axis
2006	Bisgaard *et al.* [7]	Bifurcation model of an axisymmetric incompressible bubble off the axis

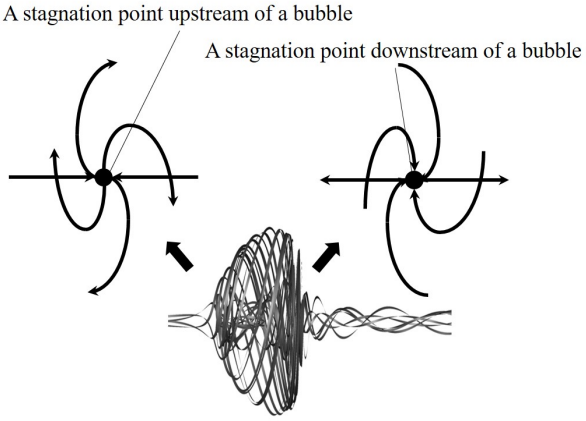

Figure 1.5: Saddle foci around a recirculating flow region

The local bifurcation on an axisymmetric bubble-type vortex breakdown was firstly analyzed by Brøns *et al.* [13]. They used a Stokes' stream function which is a stream function of an axisymmetric flow and derived a simple nonlinear dynamical system in which a bubble-type vortex breakdown is yielded from a swelling longitudinal vortex as shown in Fig. 1.6. It is written in cylindrical coordinates as

$$\frac{d}{dt}r = -rz, \tag{1.4}$$

$$\frac{d}{dt}z = \mu + r^2 + \frac{1}{2}z^2, \tag{1.5}$$

where μ is a bifurcation parameter. If μ is larger than zero, there exist a recirculating flow region, while there doesn't exist any recirculating flow region if μ is smaller than zero. By this group, topological patterns of the axisymmetric bubble-type vortex breakdown off the axis were also revealed [7].

It can be said that the topological patterns of the flow field with an axisymmetric bubble-type vortex breakdown has been well understood for an incompressible flow so far. The next problem

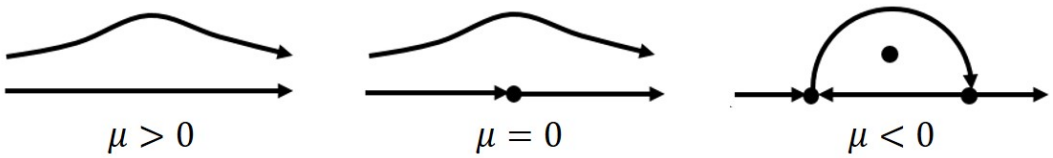

Figure 1.6: Topological bifurcation of axisymmetric and incompressible bubble-type vortex breakdown

was how the topology changes under nonaxisymmetry and compressibility. The influence of the nonaxisymmetry on the topology was much more investigated than that of the compressibility because it strongly connected to chaos and essentially appeared in visualization results of experiments mainly in a closed cylinder with a rotating bottom [67].

It was known that chaotic advection of particle traces was observed as *finger-like* structure around a recirculaitng flow region for a periodic bubble-type vortex breakdown in a visualization experiment by Escudier [19]. Holmes theoretically showed that time-periodic axisymmetric perturbations was able to yield Lagrangian chaos including the chaotic particle traces [31]. Lopez and Perry numerically showed the particle traces of periodic axisymmetric solutions were chaotic with finger-like structure in a Poincaré section visualized in the experiment [38].

However, this finger-like structure in the Poincaré section was not only for periodic axisymmetric flows but also for steady nonaxisymmetric flows. Spohn *et al* experimentally showed the finger-like structure of the particle traces was observed around a stagnation point downstream of a recirculating flow region even for steady flows. Sotiropoulos and Ventikos numerically found their solutions for a fully three-dimensional flow in the same configuration as the experiments also yielded the chaotic structure in the Poincaré section [57]. In another article by Sotiropoulos *et al.* [58], they concluded that the Shilnikov bifurcation [56], which was known as a chaotic bifurcation of an aaxisymetric flow, can take place for the vortex breakdown in the closed cylinder. Brøns *et al.* numerically showed imperfections of the experimental setup caused such a bifurcation [11]. Also, it was shown that diffusive particle traces were able to yield similar pictures to the visualization results [12].

In contrast to a lot of studies on the chaotic advection of the vortex breakdown in the closed cylinder, the chaotic feature of asymmetric recirculating flow region in other geometries were not investigated well. There exists a three-dimensional investigation but it mainly focused on vorticity dynamics [59]. As a next step, we need to look for these chaotic topologies in other configurations. Then, in this thesis, the asymmetric recirculating flow region is numerically investigated in a swirling jet from the aspect of the chaotic property.

Also, an influence of the compressiblity is not known yet. For now, it is assumed that there is no influence of the compressibility on the topology of the bubble-type vortex breakdown [73].

Then, in this thesis, addtional patterns of the bifurcation of the bubble-type vortex breakdown caused by the compressibility and non-axisymmetry are investigated. Appliying the above analyses to data obtained by numerically simulating Navier-Stokes equations, we comprehensively examine the topology of the bubble-type vortex breakdown.

1.2 Stability of bubble-type vortex breakdown

A flow stability explains how a small perturbation behaves both in time and in a space when a prescribed flow is given. Starting from a famous pipe experiment by Reynolds [50], there is a long history of tremendous research on the flow stability. In this section, we at first look back at fundamental configuration and previous studies on the flow stability picking up some review papers. Secondly, we focus on the stability of a vortex breakdown. We see what was revealed so far from previous studies on the stability of the vortex breakdown. After that, what we investigate in this thesis is shown.

1.2.1 Stability analysis

Consider governing equations of a fluid motion: they are often nonlinear partial differential equations (PDEs) like Navier-Stokes equations. Here, we denote them as

$$\partial_t \mathbf{q} = \mathcal{N}\mathbf{q}, \tag{1.6}$$

where $\mathbf{q}$ is a variable vector and $\mathcal{N}$ is a nonlinear operator. When we directly analyze a development in time of a solution of Eq. 1.6, it is nonlinear stability analysis, but it is often quite hard to analyze it. If $\bar{\mathbf{q}}$ such that $\mathcal{N}\bar{\mathbf{q}} = \mathbf{0}$ exists, $\bar{\mathbf{q}}$ is a steady solution of Eq. 1.6. It is called *base flow* in many literature. Then infinitesimal perturbations of the variable vector $\mathbf{q}'$ such that $\mathbf{q} = \bar{\mathbf{q}} + \mathbf{q}'$ can be introduced. We can linearize Eq. 1.6 about $\mathbf{q}'$ as

$$\frac{d}{dt}\mathbf{q}' = \mathcal{L}\mathbf{q}', \tag{1.7}$$

where $\mathcal{L}$ is a linearized operator of $\mathcal{N}$ around $\bar{\mathbf{q}}$. When we analyze the development in time of a solution of Eq. 1.7, it is linear stability analysis.

On a linear stability analysis, we consider the spectral decomposition of $\mathcal{L}$. There are mainly two approaches to analyze the flow stability. One is local stability anaysis and the other is global stability analysis. Difference between them is briefly showed here. For more detail, see a review paper by Huerre and Monkewitz [32].

On the local stability analysis, a perturbation is assumed to be a plainwave, say x. Then we need to assume the base flow is parallel. Also, we consider the perturbation can be written as a

wave-like solution which is an exponential function of both time and the direction x:

$$\mathbf{q}' = \breve{\mathbf{q}} e^{ik_{loc}(x - c_{loc}t)}, \tag{1.8}$$

where k_{loc} is the wavenumber of the perturbation and c_{loc} is the wave speed of the perturbation. Substituting Eq. 1.8 into Eq. 1.7, we can reduce the original equation and solve an eigenproblem and obtain k_{loc} and c_{loc}. For a two-dimensional viscous parallel flow such as Poiseuille flow, the reduced equation is named Orr-Sommerfeld equation [44]. $-k_{loc}c_{loc}$ is the eigenfrequency. The real part of the stability $\mathcal{R}(-ik_{loc}c_{loc})$ is a growth rate and the imaginary part of the stability $\mathcal{I}(-ik_{loc}c_{loc})$ is a frequency. If $\mathcal{R}(-ik_{loc}c_{loc}) > 0$, the flow is unstable, while it is stable if $\mathcal{R}(-ik_{loc}c_{loc}) < 0$. If the flow is parallel, the local stability analysis gives good predictions for wakes [64], jets [3], and two-phase flows [71]. However, if the flow is not parallel, it becomes difficult to apply the local stability analysis.

1.2.2 Spectrum and eigenfunction of global flow field

On the global stability analysis, the perturbation is considered as a multiply of an exponential function of time and there is no limitation to its spatially distribution. It can be written as

$$\mathbf{q}' = \hat{\mathbf{q}} e^{\lambda t}, \tag{1.9}$$

where λ is the flow stability. Substituting Eq. 1.10 into Eq. 1.7, λ becomes the eigenspectrum of $\mathcal{L}$. Considering we numerically solce this prolem, it becomes an eigenproblem of a matrix L which is discretization of the linear operator $\mathcal{L}$:

$$L\boldsymbol{\phi}_i = \lambda_i \boldsymbol{\phi}_i, \tag{1.10}$$

where λ_i is i-th eigenvalue and $\boldsymbol{\phi}_i$ is i-th eigenvector. Then, if $\mathcal{R}(\lambda) > 0$, the flow is unstable, while it is stable if $\mathcal{R}(\lambda) < 0$. $\boldsymbol{\phi}_i$ is a global mode which shows where the perturbation globally develops. This global stability analysis can be applied to even a non-parallel flow. Then, it is gathering attention to the global stability analysis these days, as computational power advances.

1.2.3 Spectrum and eigenfunction of adjoint flow field

More recently, the stability of the adjoint system of flow equations is becoming to be analyzed [22]. When we have an operator, there exists an adjoint operator. Denoting an inner product as $\langle \cdot, \cdot \rangle$, the adjoint operator $\mathcal{L}^*$ of the original one $\mathcal{L}$ satisfies a following relation:

$$\langle \mathcal{L}\mathbf{f}, \mathbf{g} \rangle = \langle \mathbf{f}, \mathcal{L}^*\mathbf{g} \rangle. \tag{1.11}$$

For example, transposing a matrix and taking its conjugate pair, we get an adjoint matrix. When we solve the eigenvalue problem, it is worth to obatin not only eigenvectors but also adjoint eigenvectors. It is called *adjoint-based analysis*. Solving the eigenvalue problem of the adjoint matrix L^*, we obtain the conjugate eigenvalues of the direct matrix L and the adjoint eigenvectors $\boldsymbol{\psi}_i$. They are connected by the following relation:

$$L^*\boldsymbol{\psi}_i = \bar{\lambda}_i\boldsymbol{\psi}_i, \tag{1.12}$$

where $\boldsymbol{\psi}_i$ is i-th eigenvector of L^*. $\boldsymbol{\psi}_i$ is also a global mode which shows where the perturbation develops in the adjoint system. In many literature, $\boldsymbol{\psi}_i$ is called *adjoint mode*, while $\boldsymbol{\phi}_i$ is called *direct mode*.

Adjoint-based analysis reveals *receptivity* of a base flow. We see the receptivity in studies on laminar-turbulent transtion [30]. In the area of these studies, perturbations are inevitably produced from enviromental or controlled disturbances. The receptivity phase consists of the transformation from the disturbances to the perturbations. The receptivity has the sources such as the enviroment or the flow control. They are explained in detail at Chapter 2 but, in this thesis, three receptivities are used: receptivities to a mass injection, to an external forcing, and an external heating. Giannetti and Luchini [24], who originally introduced the adjoint-based analysis, defined another receptivity, which is to spatially localized feedbacks, called *sensitivity*. The sensitivity tells us an internal feedback mechanism of the base flow and it is defined as

$$\zeta \equiv \frac{\|\boldsymbol{\psi}_i\|\|\boldsymbol{\phi}_i\|}{|\langle\boldsymbol{\psi}_i, \boldsymbol{\phi}_i\rangle|}. \tag{1.13}$$

The sensitivity is a scalar function indicating where the pertubation is highly amplified. In another paper by Giannetti and Luchini [22], they showed the receptivities and the sensitivity around a circular cylinder and the sensitivity was high around the dividing streamlines of a pair of twin vortices. Then, they concluded that the shear layer region had the largest sensitivity and it meant feedback mechanism to amplify the perturbation was along the shear layer. The adjoint-based analysis is the state of the art of the stability analysis and new receptivities are still defined and invesitigated [41].

1.2.4 Previous studies on bubble-type vortex breakdown

Next, we focus on what has been understood about vortex breakdowns by the stability analysis so far. The flow stability plays an important role on the bubble-type vortex breakdown in two senses. In one sense, the onset of the bubble-type vortex breakdown is caused by a stability breaking. It was an open problem since Benjamin [4, 5], but Wang and Rusak [68] theoretically showed that there exists a stable bubble-type solution and it can take place when a colmunar-vortex solution become unstable. In another sense, the onset of a spiral-type vortex breakdown can be also caused

by the stability breaking. We can say this research is the mainstream of the research on the vortex breakdown these days. Some researches say that its onset corresponds to the stability breaking of the bubble-type vortex breakdown. In this study, this side is focused on, and then, those previous studies are reviewed below.

Some of previous studies are extracted and summarized in Table 1.2.

Table 1.2: Review of stability analysis on vortex breakdown

Year	Group	Contents
2003	Ruith *et al.* [52]	Direct numerical simulation of swirling jets and wakes
2006	Gallaire *et al.* [21]	Local stability analysis on incompressible bubble
2011	Meliga and Gallaire [42]	Global stability analysis on incompressible bubble
2013	Qadri *et al.* [49]	Sensitivity analysis on axisymmetric and incompressible bubble

First of all, the onset of the spiral-type vortex breakdown was not attributed to stability breaking because the flow field was too complicated to analyze the stability. Ruith *et al.* [52], however, conducted a direct numerical simulation (DNS) of a swirling jet and showed that transition from a stedy bubble-type vortex breakdown to a periodic spiral-type vortex breakdown takes place like transition from a steady twin vortex to a periodic emission of Kármán vortices [35]. Then, it became considered that the stability breaking of the bubble-type vortex breakdown resulted in the onset of the spiral-type vortex breakdown. Based on this DNS, the local stability analysis was done by Gallaire *et al.* [21]. They showed there were two locations where the flow becomes convectionally unstable and one of the local frequencies at the two locations agreed well with a global frequency of the flow field observed by the DNS. That was at the wake of the recirculating flow region. Then, they concluded the transition to the spiral-typ vortex breakdown was attributed to the stability breaking at the wake of the bubble-type vortex breakdown. Next, the global stability analysis was done by Meliga and Gallaire [42]. They showed a global mode of the bubble-type vortex breakdown and a perturbation developed at the wake of the recirculating flow region. Recently, the sensitivity of the bubble-type vortex breakdown was analyzed by Qadri *et al.* [49]. They found a case where the sensitivity upstream of the recirculating flow region was higher than that at the wake of the recirculating flow region. Then, they concluded that the transition to the spiral-type vortex breakdown was caused by both the centrifugal instability mechanism upstream of the recirculating flow region and the Kelvin-Helmholtz instability mechanism at the wake.

As shown above, the stability mechanism of the bubble-type vortex breakdown has been understood well. Previous studies, however, assumed the base flow was axisymmetric. As discussed in the last section, the axisymmetric topology of the bubble-type vortex breakdown can be easily violated and chaotic bifurcation can take place because of a asymmetric perturbation. It is sure that the asymmetric recirculating flow region is observed in a real experiment and this is a gap to be filled. Then, as a next step, we need to investigate how the stability mechanism or structure

changes when the base flow becomes asymmetric. In this thesis, we analyze the global stabilities of asymmetic bubble-type vortex breakdowns obtained by CFD.

1.3 Contribution of this thesis

We have reviewed what has been known and what remains to be studied about the bubble-type vortex breakdown in the foregong sections. In resoponse to them, research objectives in this thesis are as follows.

- To reveal topologies of the bubble-type vortex breakdown for unsteady, fully three-dimensional compressible.flows.

- To reveal global stabilities, receptivities, and sensitivities of the bubble-type vortex breakdown for fully three-dimensional compressible flows.

As a result, this thesis contributes to both the topology and the stability of the bubble-type vortex breakdown. Chapter 4 presents an eigenvalue analysis and a local bifurcation analysis on the bubble-type vortex breakdown from an aspect of the equation of streamlines. The main contributions of this study are as follows.

- From the eigenvalue analysis of a velocity gradient tensor at a stagnation-point pair of a bubble-type vortex breakdown, its topological structure is comprehensively revealed from its onset for various configurations at Section 4.4.1 through Section 4.4.3.

- Simulating an unsteady compressible flow with a vortex breakdown, it is newly found that there exist additional bifurcations of the topology of axisymmetric recirculating flow regions for instananeous streamlines of the vortex breakdown at Section 4.4.2.

- Introducing an asymmetric parameter to an axisymmetric swirling jet, an asymmetic compressible bubble-type vortex breakdown is numeically obtained and chaotic structure is obtained in a Poincaré section at Section 4.4.3.

Chapter 5 presents a global stability analysis and an adjoint-based analysis on the buble-type vortex breakdown from an aspect of the equation of motion. The main contributions of this study are as follows.

- Analyzing a global stability on a compressible bubble-type vortex breakdown for linearized Navier-Stokes equations, the global mode for thermodynamical variables as well as kinematic variables is revealed at Section 5.5.1.

- Also analyzing the global stability for adjoint equations, a receptivity to an external heating is revealed at Section 5.5.1.
- Analyzing a sensitivity of an asymmetric compressible bubble-type vortex breakdown, a relation between the high sensitivity region and the topological structure of streamlines is newly obtained at Section 5.5.2.

Finally, Fig. 1.7 shows the research table of this thesis with what was already investigated, what is not yet, and what is invetigated in this thesis by a table of assumptions versus two keywords (aspects) as important properties of the bubble-type vortex breakdown.

1.4 Organization of this thesis

Chapter 2 presents background theories in this thesis. Chapter 3 presents computational configurations and methods. Chapter 4 and Chapter 5 are main results. Chapter 4 presents the study on the topology of the bubble-type vortex breakdown. Chapter 5 presents the study on the stability of the bubble-type vortex breakdown. At last, Chapter 6 provides concluding remarks.

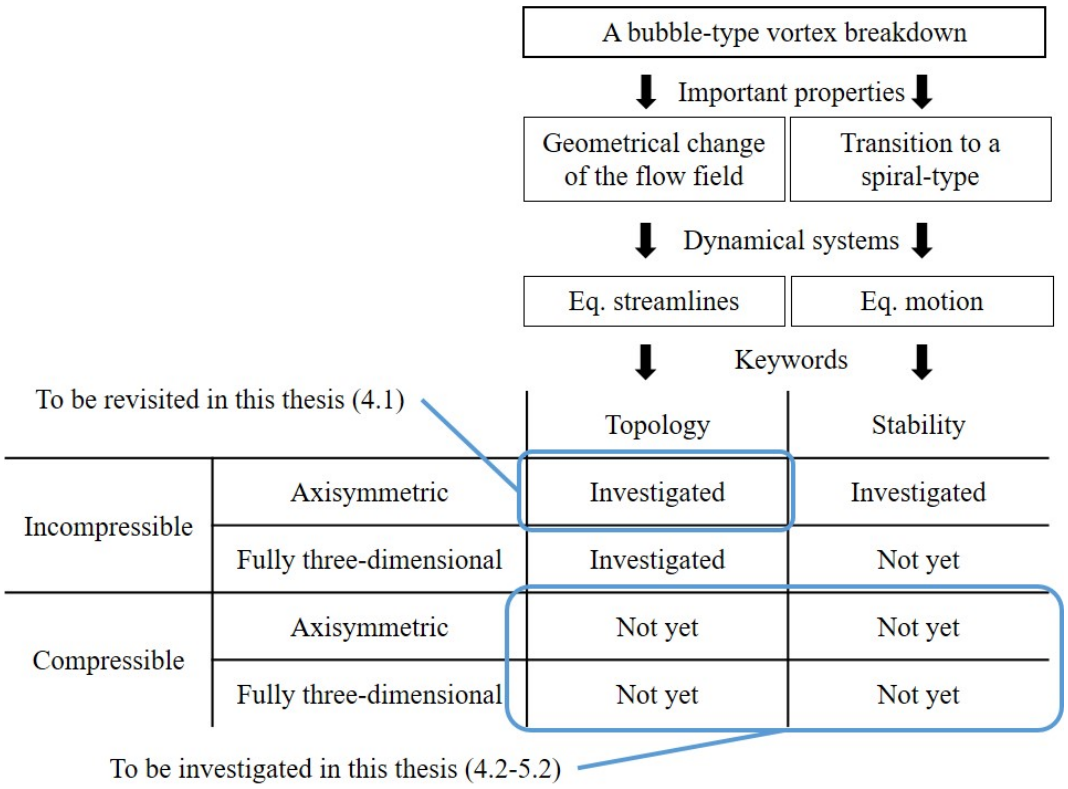

Figure 1.7: Two aspects and what is investigated in this thesis from these aspects

Chapter 2

Background Theories

In this chapter, theories applied to analyze topologies and stabilities of bubble-type vortex breakdowns. Fig. 2.1 shows the research table and where each theory plays a role in this thesis.

2.1 Local bifurcation theory

In this section, we explain about methods for the topological analysis of streamlines of the bubble-type vortex breakdown. The methods are

- Eigenanalysis of a velocity gradient tensor at a stagnation point.
- Weakly nonlinear bifurcation analysis.

2.1.1 Eigenanalysis of velocity gradient tensor

Velocity gradient tensor

Consider a dynamical system of streamlines. It is rewritten as

$$\frac{d}{dt}\mathbf{x} = \mathbf{u}(\mathbf{x}).$$

$\mathbf{u}$ is a velocity vector and a vector function of $\mathbf{x}$. If it is linearized at a fixed point,

$$\frac{d}{dt}\mathbf{x} = A\mathbf{x}, \tag{2.1}$$

where A is a Jacobian matrix called *velocity gradient tensor*.

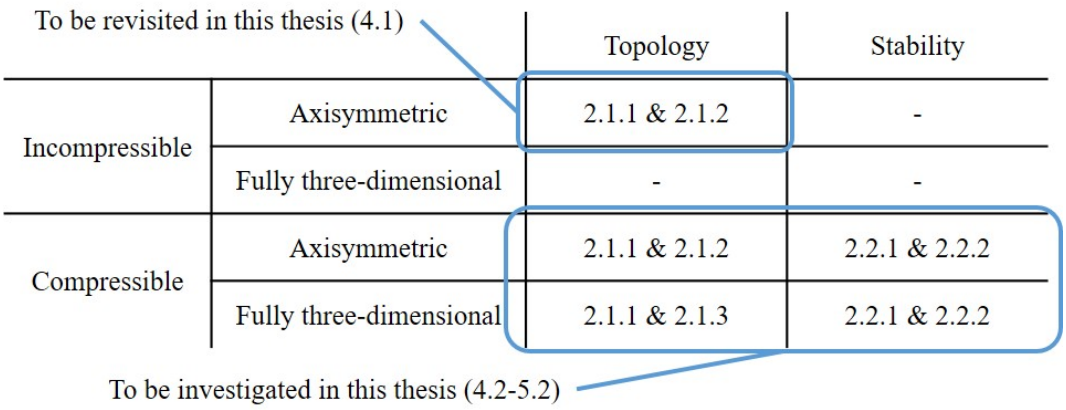

Figure 2.1: Research table and where each theory plays a role in this thesis

As introduced in Chapter 1, the eigenproblem of the velocity gradient tensor A at a fixed point is the most fundamental property on the topological analysis of the dynamical system of streamlines. In this thesis, we also begin from this analysis. It is already known that a pair of stagnation points which bound a bubble-type vortex breakdown are both saddle foci. We investigate this structure for various parameters from its onset and we see the existence of a non-hyperbolic fixed point. The non-hyperbolic fixed point has a velocity gradient tensor whose eigenvalues have at least zero-real-part. Such a fixed point is quite important to analyze a bifurcation phenomenon.

Calculation methodology

The velocity gradient tensor at the stagnation-point pair is calculated from CFD data. At first, the location of the stangation point is represented by the grid point where the velocity magnitude is the smallest. Next, the differential terms are calculated by the 2nd order central difference using neighbor grid points.

2.1.2 Weakly nonlinear bifurcation analysis

Non-hyperbolic fixed point

As shown in Chapter 1, a one-parameter bifurcation model of streamlines for the onset of an incompressible axisymmetric bubble-type vortex breakdown was obtained by Brøns *et al.* [13]. In mathematics, a two-parameter bifurcation model including the one-parameter model was considered and its possible patterns of the bifurcation were examined by Guckenheimer and Holmes [27].

In this subsection, we introduce a method which derives the two-parameter model and see how many patterns are mathematically possible.

The key to analyze the bifurcation patterns is the non-hyperbolic fixed point introduced at the last subsection. When the non-hyperbolic fixed point exists, the structure of streamlines around the fixed point is easily influenced by nonlinear terms. For example, following system has a non-hyperbolic fixed point at the origin:

$$\frac{d}{dt}\mathbf{x} = \begin{pmatrix} 0 & -1 \\ 1 & 0 \end{pmatrix} \mathbf{x} + \mu \begin{pmatrix} x^3 \\ y^3 \end{pmatrix}, \tag{2.2}$$

where μ is a parameter. When we analyze the eigenvalues of the velocity gradient tensor at the fixed point, the fixed point is classified to a center. Streamlines around the fixed point, however, are attractected to the fixed point when $\mu < 0$ and repelled from the fixed point when $\mu > 0$. It means a bifurcation phenomenon takes place and μ is a bifurcation parameter. Then, when we observe the non-hyperbolic fixed point, it means the bifurcation phenomenon can take place by a slightly change in bifurcation parameters.

Normal form

When there exists a non-hyperbolic fixed point in a dynamical system, we can narrow down the patterns of streamlines around it by its velocity gradient tensor. One of the simplest forms which describe the dynamical system of streamlines around the fixed point is called *normal form* [69]. A normal form has the least numbers of nonlinear terms. The nonlinear terms are derived from the normal form theorem. Actually, the velocity gradient tensor obtained in this thesis is very simple, and then, the normal form is already known by Guckenheimer and Holmes [27]. It is written as

$$\frac{dr}{dt} = a_1 r z, \tag{2.3}$$

$$\frac{dz}{dt} = b_1 r^2 + c_1 z^2, \tag{2.4}$$

$$\frac{d\theta}{dt} = \omega, \tag{2.5}$$

where a_1, b_1, c_1, and ω are coefficients, which characterize the topological structure of streamlines around the non-hyperbolic fixed point. Under the axisymmetry, θ is independent to the other variables. Then, there is no influence on the topology of the streamlines by θ. Transforming the coordinate system in order to reduce the combination of the coefficients

$$\check{r} = \sqrt{|b_1 c_1|}\, r, \tag{2.6}$$

$$\check{z} = c_1 z, \tag{2.7}$$

$$a = a_1 c_1, \tag{2.8}$$

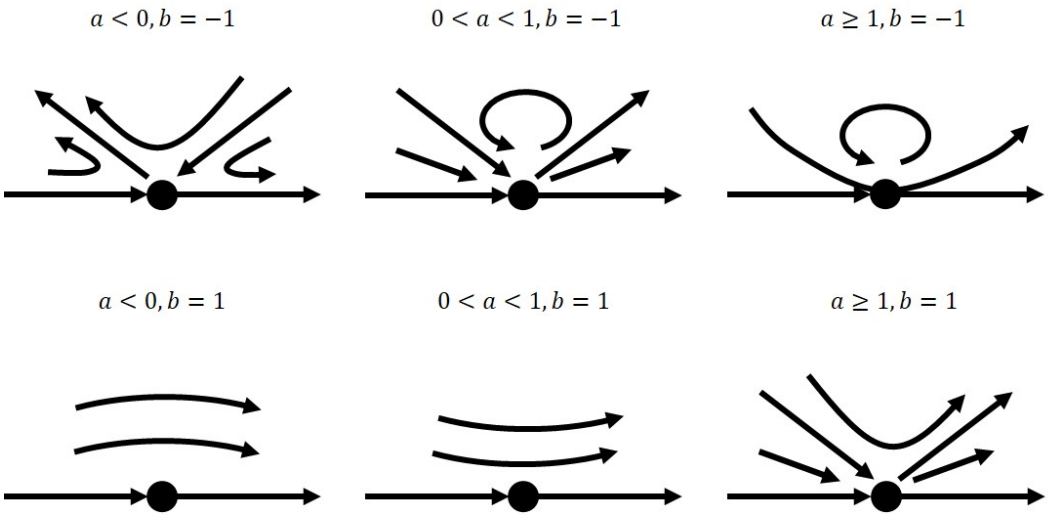

Figure 2.2: Topological patterns of the non-hyperbolic fixed point

we can rewrite Eqs. 2.5 as

$$\frac{d\check{r}}{dt} = a\check{r}\check{z}, \tag{2.9}$$

$$\frac{d\check{z}}{dt} = b\check{r}^2 + \check{z}^2, \tag{2.10}$$

where $b = \pm 1$.

It is worth to mention that the topogy in $\check{r}\check{z}$-plane is same as that in rz-plane. There are six patterns of the streamlines for various a and b as shown in Fig. 2.2. The case of the onset of a bubble-type vortex breakdown is the case for $a < 0$ and $b = 1$.

Two-paramter model

The non-hyperbolic fixed point also tells us how many parameters can change the topological patterns of the local dynamical system around the fixed point. According to Guckenheimer and Holmes [27], the number of parameters is two. By some mathematical manipulations, we can add two parameters to the normal form. One of the forms is written in cylindrical coordinates as

$$\frac{d\check{r}}{dt} = \mu_1\check{r} + a\check{r}\check{z}, \tag{2.11}$$

$$\frac{d\check{z}}{dt} = \mu_2 + \check{r}^2 + \check{z}^2, \tag{2.12}$$

where μ_1, and μ_2 are bifurcation parameters.

This two-parameter model has up to three fixed points on the $\check{r}\check{z}$-plane. A pair of fixed points can exist at $(\check{r}, \check{z}) = (0, \pm\sqrt{-\mu_2})$ when $\mu_2 < 0$. They are saddles on the axis (saddlefoci in the three-dimensional space). A fixed point off the axis can exist at $(\check{r}, \check{z}) = (\sqrt{\mu_2 + \frac{\mu_1^2}{a^2}}, -\frac{\mu_1}{a})$ when $\mu_2 < -\frac{\mu_1^2}{a^2}$. It is a center, an attracting focus, or repelling focus. Taking the trace of the velocity gradient tensor at the focus, we can obtain

$$tr(A) = -\frac{2\mu_1}{a}. \tag{2.13}$$

Then, it is attracting when $\mu_1 < 0$, it is repelling when $\mu_1 > 0$, and it is a center when $\mu_1 = 0$. Fig. 2.3 shows the plot of the bifurcation patterns on the $\mu_1\mu_2$-plane.

When $\mu_1 = 0$, this model corresponds to the one-parameter model by Brøns *et al.* [13]. However, the two-parameter model indicates us additional bifurcation patterns. Those are bifurcation phenomena of a fixed point off the axis. In this thesis, the additional patterns are investigated by numerical simulations. We not only visualize the topological structure of streamlines but also fit the data on the two-parameter model and analyze the two bifurcation parameters.

Calculation methodology

In Chapter 4, the two parameters are approximately obtained by fitting CFD data to the bifurcation model. At first, the bifurcation parameters are connected to physical variables. Next, corresponding physical variables are extracted from the CFD data at the middle grid point of the locations of the pair of stagnation points.

2.1.3 Investigation of chaos

In this thesis, we investigate not only an axisymmetric bubble-type vortex breakdown but also a fully three-dimensional one. At this subsection, a few concepts to analyze the asymmetric topology are explained.

Poincaré map

A Poincaré map is defined as a sequential plot of streamlines crossing a fixed plane, which is a lower-dimensional subspace, called a Poincaré section. It becomes a discrete dynamical system on the Poincaré section and describes the map from the first point on the section to the second point. The Poincaré map preserves the dynaimcal property of the periodic orbit of the original dynamical system.

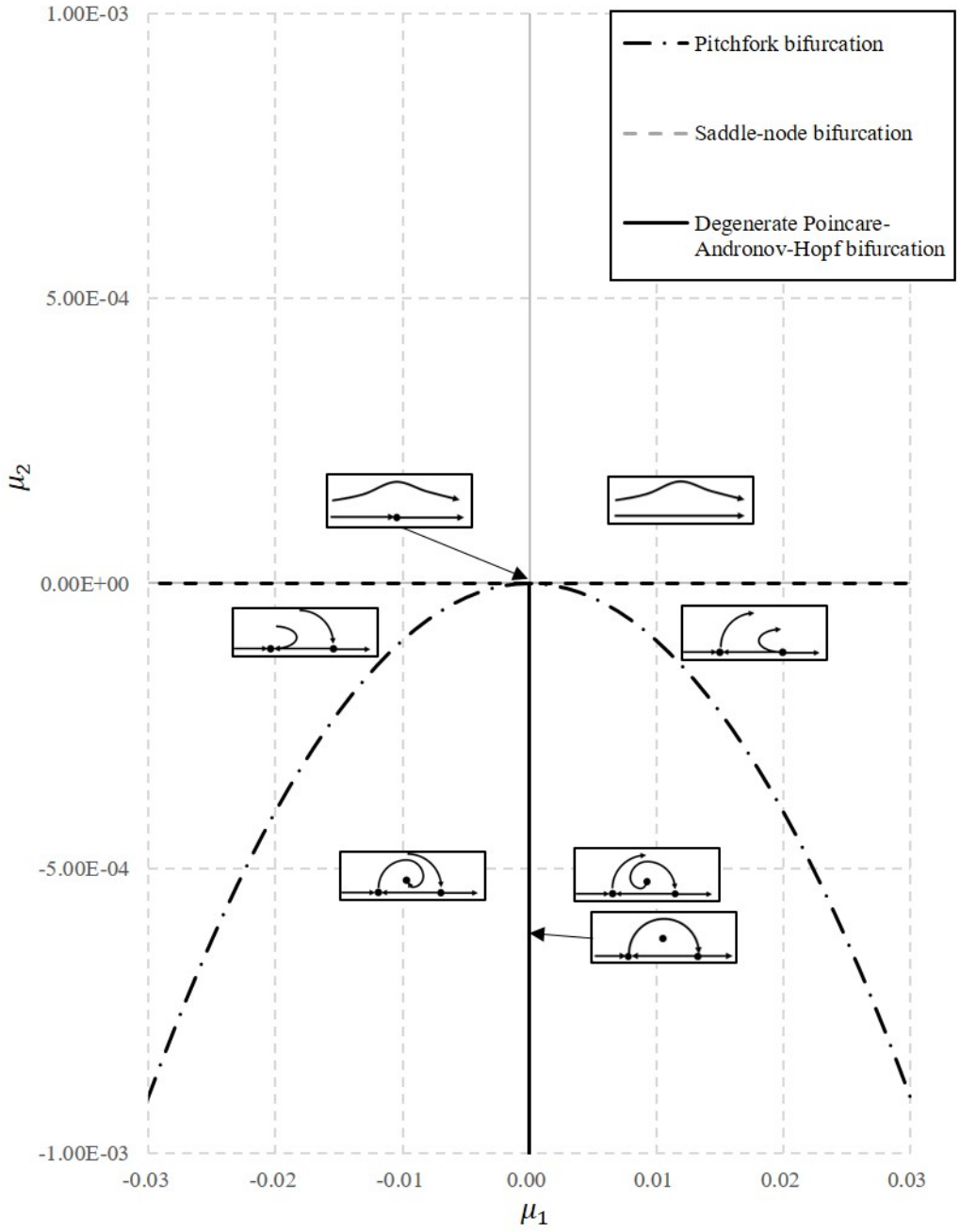

Figure 2.3: Bifurcation map of two-parameter model [27]

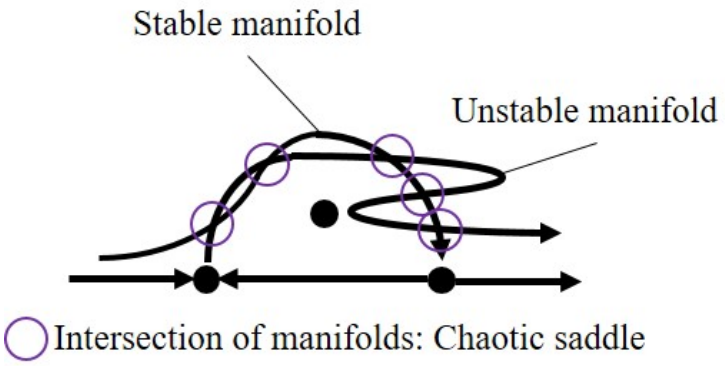

Figure 2.4: Schematics of stable and unstable manifolds [27]

In this thesis, the Poincaré map of three-dimensional streamlines is plotted on a two-dimensional plane. Actually, it is easy for us to imagine the Poincaré map of the streamlines of a bubble-type vortex breakdown because the visualization of tracer particles by a laser sheet in an experiment is that.

Stable and Unstable manifolds

In order to investigate chaotic property of streamlines, finger-like structure becomes a key. This structure is characterized by intersections of stable and unstable manifolds [20]. The stable manifold means streamlines into a stagnation point while the unstable manifold means streamlines from a stagnation point as shown in Fig. 2.4. The Poincaré map of the unstable manifold of the stagnation point upstream of the recirculating flow region corresponds to the visualization of the paricle traces put close to the stagnation point. Then, we can calculate the unstable manifold by directl integrating the equations of streamlines in time. In this thesis, the equations of streamlines are integrated by 1st-order explicit method by $\delta t = 0.01$. The stable manifold can be calculated by invertedly integrating the equations of streamlines in time. The integration method and the time width are same as those for the unstable manifold.

Calculation methodology

We see the structure of unstable and stable manifolds on a Poincaré section for an asymmetric bubble-type vortex breakdown in Chapter 4. At first, the Poincaré section is represented by a plane for $x = 0$. Next, the unstable manifold from the stagnation point upstream of the recirculating flow region is calculated by integrating a hundered non-diffusive particles along the velocity vector field

from a starting position which is set by a width between the grid points around the stagnation point. Time integration is done by the 1st order explicit method and the time width is set at $\delta t = 0.01$. At every time step, whether the orbit from the starting position cross the Poincaré section is checked and, when it crosses, the position is memorized by linearly interpolating the positions at the last and the present steps. Third, the stable manifold to the stagnation point downstream of the recirculating flow region is calculated by the same method as the unstable manifold. The diffference is only the time width which is set at $\delta t = -0.01$. By setting the time width negative, we can caluculate the stable manifold like the unstable manifold. At last, chaotic saddles are approximately calculated by looking for positions where the distance between the both manifolds are smaller than a threshold which is set as the one tenth of the minimum grid width.

2.2 Global stability theory

2.2.1 Global stability analysis

Eigenproblem of flow operator

A flow opereator $\mathcal{N}$ is consisted from all the terms other than the time derivative of the variable vector. As shown in Chapter 1, it is rewritten as

$$\partial_t \mathbf{q} = \mathcal{N}\mathbf{q}. \tag{2.14}$$

When we have a steay solution $\bar{\mathbf{q}}$, a linear dynamical system of perturbation vector $\mathbf{q}'$ can be obtained as

$$\frac{d}{dt}\mathbf{q}' = \mathcal{L}(\bar{\mathbf{q}})\mathbf{q}'. \tag{2.15}$$

Discretizing the linear operator $\mathcal{L}(\bar{\mathbf{q}})$ in a computational domain, we obatin a discretized system such that

$$\frac{d}{dt}\mathbf{q}_n^{'} = L(\bar{\mathbf{q}}_n)\mathbf{q}_n^{'}, \tag{2.16}$$

where $\mathbf{q}_n^{'}$ is a discretized variable vector in an n-dimensional space, $L(\bar{\mathbf{q}}_n)$ is an $n \times n$ matrix computed from the stedy solution $\bar{\mathbf{q}}_n$, and n is a multiple of the total grid point and the number of variables.

Solving the eigenproblem of the matrix L, we obtain i-th eigenvalue λ_i and its eigenvector $\boldsymbol{\phi}_i$. They are connected by the following relation:

$$L\boldsymbol{\phi}_i = \lambda_i \boldsymbol{\phi}_i. \tag{2.17}$$

The real and the imaginary parts of λ_i are the growth rate and frequency respectively. If the growth rate is larger than zero, the steady solution is unstable. Before introducing the method to solve this eigenproblem, we introduce how to obtain the unstabe steady solution.

Selective frequency damping method

It is impossible to obatin an unstable steady solution by normally solving the governing equations, but there are several methods to obtain the unstable steady solution. One of the methods is the selective frequency damping (SFD) method [1]. This method requires some modification of the governing equations 2.14. Modified equations are written as

$$\partial_t \mathbf{q} = \mathcal{N}\mathbf{q} - \chi_1(\mathbf{q} - \tilde{\mathbf{q}}), \tag{2.18}$$

$$\partial_t \tilde{\mathbf{q}} = \frac{\mathbf{q} - \tilde{\mathbf{q}}}{\chi_2}. \tag{2.19}$$

where χ_1 and χ_2 are positive-value parameters, and $\tilde{\mathbf{q}}$ is another varaible vector which will be a steady solution. Applying this SFD method, we can obtain $\bar{\mathbf{q}}$ even if it is unstable. Next, we show how to solve the eigenproblem of L.

Time stepping method

If $log_{10}n \approx 5$, it is becoming to be able to directly solve the eigenproblem of L with advance in computational power. Directly solving the matrix means to memorize the all components of the matrix. It is called *matrix-forming method*. If $log_{10}n > 5$, however, it is still difficult to directly solve it. Such an amount of the grid points is required for a computation of a three-dimensional flow field. Then, a method without forming the matrix, called *matrix-free method*, is used instead of the matrix-forming method. One of those methods is *time stepping method* proposed by Eriksson and Rizzi [18].

The routine of the time stepping method is briefly shown here. It doesn't solve the eigenproblem of L but solve that of a matrix $\hat{L}$ such that

$$\hat{L} \equiv Le^{\delta t}, \tag{2.20}$$

where δt is a time width of the computation. Then, $\hat{L}$ is a linear map which takes the flow state one time step further. Eigenvalues $\hat{\lambda}$ of $\hat{L}$ and the eigenvalues of L are connected by a relation such that

$$\hat{\lambda} = e^{\lambda \delta t}. \tag{2.21}$$

The time stepping method is based on a Krylov subspace method [34]. The Krylov subspace method calculates the eigenvalues $\hat{\lambda}$ and the eigenvectors $\hat{\boldsymbol{\phi}}$ on a Krylov subspace $\mathcal{K}_m(L, \mathbf{q}_0^{'})$ such that

$$\mathcal{K}_m(L, \mathbf{q}_0^{'}) = span\{\mathbf{q}_0^{'}, \hat{L}\mathbf{q}_0^{'}, \hat{L}^2\mathbf{q}_0^{'}, \cdots, \hat{L}^m\mathbf{q}_0^{'}\}, \tag{2.22}$$

where $\mathbf{q}_0^{'}$ is an initial vector which can be arbiterally chosen. From the definition of $\hat{L}$, we can rewrite $\mathcal{K}_m$ as

$$\mathcal{K}_m(L, \mathbf{q}_0^{'}) = span\{\mathbf{q}_0^{'}, \mathbf{q}_1^{'}, \mathbf{q}_2^{'}, \cdots, \mathbf{q}_m^{'}\}, \tag{2.23}$$

where $\mathbf{q}_m^{'}$ is the flow state at $t = m\delta t$ beggining from $\mathbf{q}_0^{'}$. It means computing a flow field gives a basis of $\mathcal{K}_m$. If m is large, we can consider only the modes with the eigenvalues whose real part is large, and then, we can approximate $\hat{L}^m\mathbf{q}_0^{'}$ by a linear combination of bases of $\mathcal{K}_m$. From this approximation, we solve the eigenproblem of a upper-Hessenberg $m \times m$ matrix H instead of $n \times n$ matrix $\hat{L}$. The specific form of H is shown later.

In this thesis, actual manipulation of the Krylov subspace method is done by Arnoldi method [2]. This method is an iterative method constructing an orthogonal basis of $\mathcal{K}_m$. Consider to obtain an orthogonal basis $\boldsymbol{\xi}_i$ of $\mathcal{K}_m$ by the Gram-Schmidt process. $\boldsymbol{\xi}_i$ is an orthogonal basis of $\hat{L}\boldsymbol{\xi}_i$ and coefficients to express $\hat{L}\boldsymbol{\xi}_i$ by $\boldsymbol{\xi}_i$ are elements of H. We can write $\hat{L}\boldsymbol{\xi}_i$ as

$$\hat{L}\boldsymbol{\xi}_i = \sum_{j=1}^{i-1} h_{1j}\boldsymbol{\xi}_i. \tag{2.24}$$

Then, H is

$$H = \begin{pmatrix} h_{11} & \cdots & h_{1m} \\ \vdots & \ddots & \vdots \\ 0 & \cdots & h_{mm} \end{pmatrix} \tag{2.25}$$

From the eigenvectors $\boldsymbol{\xi}_i$ of H, we can approximate the eigenvalues and the eigenvectors of the original matrix:

$$\boldsymbol{\phi}_i = \sum_{k=1}^{m} \psi_{ik}\boldsymbol{\phi}_i. \tag{2.26}$$

As m increases, we can more acculately obtain a few eigenvalues and eigenvectors. If $m \to \infty$, it has been proved that the approximated eigenvalues converge to the true eigenvalues [53]. It is enough for the stability analysis on a steady or periodic flow, because a few eigenvaules from the largest real part of λ and corresponding eigenvectors are dominant.

Calculation methodology

Using the methods introduced in the above subsections, the global stability analysis on the bubble-type vortex breakdown is conducted in Chapter 5. At first, a steady solutions are calculated by the SFD method regardless of stable or unstable solution. In this thesis, χ_1 and χ_2 are set at 0.1 and 1.5 respectively. Next, the global stability and mode are analyzed by the time stepping method. The dimension of the Krylov subspace is 500, and the integration time is set as unit. Setting the integration time longer and increasing the dimension of the Krylov subspace, the convergence of the eigenvalue becomes better, but its imaginary part depends on the inverse of the integrating time. Then, when we want to quantitatively evaluate the frequency, we need to set the integration time shorter. In the present case, instead of the unit integration time, the dimension of the Krylov

subspace is very large. Although we can obtain five hundred stabilities and modes, we only focus on the least stable stability and mode.

2.2.2 Adjoint-based analysis

The point of an adjoint-based analysis is we can obtain a scalar function indicating an influence on the eigenvalue.

Eigenproblem of adjoint flow opertor

As shown in Chapter 1, when we have an operator, there exists its conjugate transpose, called an adjoint operator. Denoting an inner product as $\langle \cdot, \cdot \rangle$, the conjugate transpose $\mathcal{L}^*$ of the original operator $\mathcal{L}$ is defined as an operator which satisfies a following relation:

$$\langle \mathcal{L}\mathbf{f}, \mathbf{g} \rangle = \langle \mathbf{f}, \mathcal{L}^*\mathbf{g} \rangle. \tag{2.27}$$

This inner product is an interral in the whole domain but an integrand is not straightforward. Then this is discussed in detail in Appendix A. For the case of the discretized matrix $L(\mathbf{q}_n)$, it becomes the eigenproblem of the adjoint matrix $L^*(\mathbf{q}_n)$. Solving the eigenproblem of the adjoint matrix L^*, we obtain the conjugate eigenvalues of the direct matrix L and the adjoint eigenvectors $\boldsymbol{\psi}_i$. They are connected by the following relation:

$$L^*\boldsymbol{\psi}_i = \bar{\lambda}_i \boldsymbol{\psi}_i. \tag{2.28}$$

In this thesis, we apply the time stepping method to solve the adjoint eigenproblem. Then, we need adjoint flow equations. They are specifically shown in Chapter 3.

Sensitivity

The adjoint mode yields receptivities to various disturbances. The receptivity to a disturbance is often used in the transition process as *receptivity phase* [30]. This phase is the initial stage of the transition process consisting the transformation from the disturbance into a perturbation. When we consider a flow control, we need to know where we should put disturbances by a mass injection, an external forcing, an external heating, and so on. Then, Giannetti and Luchini [22] defined the receptivities to the above disturbances by considering how the global mode $\boldsymbol{\phi}_i$ changes by adding the disturbances. Denoting the disturbances added to the governing equations as $\boldsymbol{\epsilon}$ and the perturbed mode as $\delta\Lambda\boldsymbol{\phi}_i$,

$$\langle L\boldsymbol{\phi}_i + \boldsymbol{\epsilon}, \boldsymbol{\psi}_i \rangle = \langle (\lambda_i + \delta\Lambda)\boldsymbol{\phi}_i, \boldsymbol{\psi}_i \rangle. \tag{2.29}$$

Through some manipulations, we arrive at

$$\langle \boldsymbol{\epsilon}, \boldsymbol{\psi}_i \rangle = \delta\Lambda \langle \boldsymbol{\phi}_i, \boldsymbol{\psi}_i \rangle. \tag{2.30}$$

Then, the global mode's amplitude $\delta\Lambda$ can be written as

$$\delta\Lambda = \frac{\langle \boldsymbol{\epsilon}, \boldsymbol{\psi}_i \rangle}{\langle \boldsymbol{\phi}_i, \boldsymbol{\psi}_i \rangle}. \tag{2.31}$$

Denoting $\boldsymbol{\epsilon} = (\rho_\epsilon, \mathbf{m}_\epsilon, p_\epsilon)$ and $\boldsymbol{\psi}_i = (\rho_i^*, \mathbf{m}_i^*, p_i^*)$,

$$\delta\Lambda = \frac{\int_V \rho_\epsilon \bar{p}_i^* dV + \int_V \mathbf{m}_\epsilon \cdot \bar{\mathbf{m}}_i^* dV + \int_V p_\epsilon \bar{\rho}_i^* dV}{\langle \boldsymbol{\phi}_i, \boldsymbol{\psi}_i \rangle}. \tag{2.32}$$

Each term in the right hand side of Eq. 2.32 is the effect on the global stability from each disturbance. For examle, consider the first term of the right hand side of Eq. 2.32. Evaluating this term by the triangular inequality,

$$\frac{\int_V \rho_\epsilon \bar{p}_i^* dV}{\langle \boldsymbol{\phi}_i, \boldsymbol{\psi}_i \rangle} < \frac{\int_V |\rho_\epsilon||p_i^*| dV}{|\langle \boldsymbol{\phi}_i, \boldsymbol{\psi}_i \rangle|}. \tag{2.33}$$

The receptivity to the mass injection is $|p_i^*|$. When this value is high at some regions, the effect of the mass injection on the global stability can be high. As well as $|p_i^*|$, the receptivities to the external forcing and to the external heating are $|\mathbf{m}_i^*|$ and $|\rho_i^*|$ respectively.

When we get known where the perturbation is yielded, we want to know where the perturbation is amplified. Giannetti and Luchini [22] also defined another receptivity to spatially localized feedbacks, in another name, *sensitivity*. The sensitivity tells us where the perturbation is amplified by the internal feedback mechanism of the system. We can derive the sensitivity by the alomost same way for the above receptivities. Consider a case where the linear system of Eq. 2.16 is perturbed and the system matrix L changes to

$$L \mapsto L + \delta L. \tag{2.34}$$

By this perturbation, i-th eigenvalue λ_i also changes to

$$\lambda_i \mapsto \lambda_i + \delta\lambda_i. \tag{2.35}$$

There is a relation between Eq. 2.34 and Eq. 2.35 such that

$$(L + \delta L)\boldsymbol{\phi}_i = (\lambda_i + \delta\lambda_i)\boldsymbol{\phi}_i. \tag{2.36}$$

Taking an inner product of Eq. 2.36 and i-th adjoint mode $\boldsymbol{\psi}_i$,

$$\langle (L + \delta L)\boldsymbol{\phi}_i, \boldsymbol{\psi}_i \rangle = \langle (\lambda_i + \delta\lambda_i)\boldsymbol{\phi}_i, \boldsymbol{\psi}_i \rangle. \tag{2.37}$$

Through some manipulations, we arrive at

$$\langle \delta L\boldsymbol{\phi}_i, \boldsymbol{\psi}_i \rangle = \langle \delta\lambda_i\boldsymbol{\phi}_i, \boldsymbol{\psi}_i \rangle. \tag{2.38}$$

Then, the variation of the i-th eigenvalue can be obtained as

$$\delta\lambda_i = \frac{\langle \delta L\boldsymbol{\phi}_i, \boldsymbol{\psi}_i \rangle}{\langle \boldsymbol{\phi}_i, \boldsymbol{\psi}_i \rangle}. \tag{2.39}$$

When we consider δL is localized in the space such that

$$\delta L = C\delta(\mathbf{x} - \boldsymbol{\xi}), \tag{2.40}$$

the above equation reduces to

$$\delta\lambda_i = \frac{[C\boldsymbol{\phi}_i(\boldsymbol{\xi})] \cdot \boldsymbol{\psi}_i(\boldsymbol{\xi})}{\langle \boldsymbol{\phi}_i, \boldsymbol{\psi}_i \rangle}. \tag{2.41}$$

From the triangle inequality, we can separate C from $\boldsymbol{\phi}_i$

$$|\delta\lambda_i| < \|C\| \frac{\|\boldsymbol{\phi}_i(\boldsymbol{\xi})\| \|\boldsymbol{\psi}_i(\boldsymbol{\xi})\|}{|\langle \boldsymbol{\phi}_i, \boldsymbol{\psi}_i \rangle|}, \tag{2.42}$$

where $\|C\|$ is a Frobenius norm of the matrix C such that

$$\|C\| = \sqrt{\sum_{i=1}^{n}\sum_{j=1}^{n} c_{ij}^2}. \tag{2.43}$$

Then, the sensitivity function $\zeta(\mathbf{x})$ is

$$\zeta(\mathbf{x}) = \frac{\|\boldsymbol{\phi}_i(\mathbf{x})\| \|\boldsymbol{\psi}_i(\mathbf{x})\|}{|\langle \boldsymbol{\phi}_i, \boldsymbol{\psi}_i \rangle|}, \tag{2.44}$$

A high sensitivity region is called *wavemaker*, where the perturbation is amplified [22]. In this thesis, we investigate the sensitivity of the bubble-type vortex breakdown.

Calculation methodology

The methodology of the adjoint-based analysis is same as that of the global stability analysis. After obtaining adjoint modes, the receptivitier incuding the sensitivity are calculated.

Chapter 3

Flow Configurations and Computational Methods

Fig. 3.1 shows the research table and where each computation is used in this thesis.

In this dissertation, vortex breakdowns in two configurations are numerically simulated. One is a confined flow in a closed cylinder with a rotating bottom (called *CC*), and the other is an unconfined flow, a swirling jet laterally surrounded by free-slip boundaries (called *SJ*). Here, computational configurations and methods for these configurations are described.

In this thesis, incompressible flows and low-Mach-number approximated (LMN) flows are simualted for *CC* case. We investigate stable steady solutions for incompressible flows and unsteady solutions for LMN flows. Then, for convinience, the former is labelled as *CC-Incomp* and the latter is labelled as *CC-LMN*. Also, for *SJ* case, fully three-dimensional compressible flows are numerically simulated and we labell this as *SJ-Comp*. Computational methods applied to these flows are explained below.

3.1 Flow in closed cylinder with rotating bottom

Consider a fluid is filled in a closed cylinder. When one of the covers starts rotating, the viscosity creates a rotational flow near the rotating cover. The rotational flow moves to the sidewall by the centrifugal force, and it subsequently moves to the static cover along the sidewall. Around the static cover, the rotational flow gathers to the center of the cover, and then, a longitudinal vortex is created along the center axis of the cylinder. The longitudinal vortex moves from the static cover to the rotating one, and the flow moves to the sidewall again. This is one of the scinarios of the flow in the *CC*-configuration.

Vogel [67] found a sphere-like recirculating region along the axis of the longitudinal vortex for some rotational speeds. This phenomenon was comprehensively investigated by Escudier [19]. He

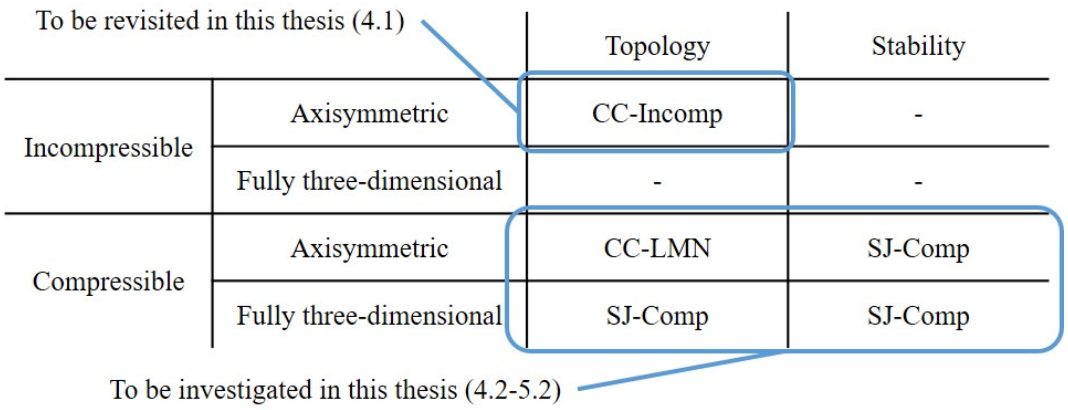

Figure 3.1: Research table and where each computation is used in this thesis

conducted experiments by controlling two parameters, an aspect ratio (a height-to-radius ratio of the cylinder) and the Reynolds number defined by the viscosity, the cover's radius, and its angular velocity. Experimental results showed highly axisymmetic and steady bubble-type vortex breakdown exists within a wide range of the parameter space as shown in Fig. 3.2. There are two parameters: one is a height-to-radius ratio of the cylinder $\frac{H}{R}$, the other is a rotational Reynolds number Re. It is defined as

$$Re = \frac{R^2\Omega}{\nu}. \tag{3.1}$$

This figure shows there are steady solutions with up to three bubble-type vortex breakdowns.

Not only experimental researches but also numerical researches have been done for the *CC*-configuration. Lopez [37] showed the location and the size of the recirculating flow region of numerical results by computing axisymmetic Navier-Stokes equations are in very good agreement with those of the experimental results.

Advantages of numerical simulations in the *CC*-configuration are sammarized as follows.

- The structure of the vortex breakdown is simple.
- Steady solutions exist.
- Computational results are in good agreement with experimental results.

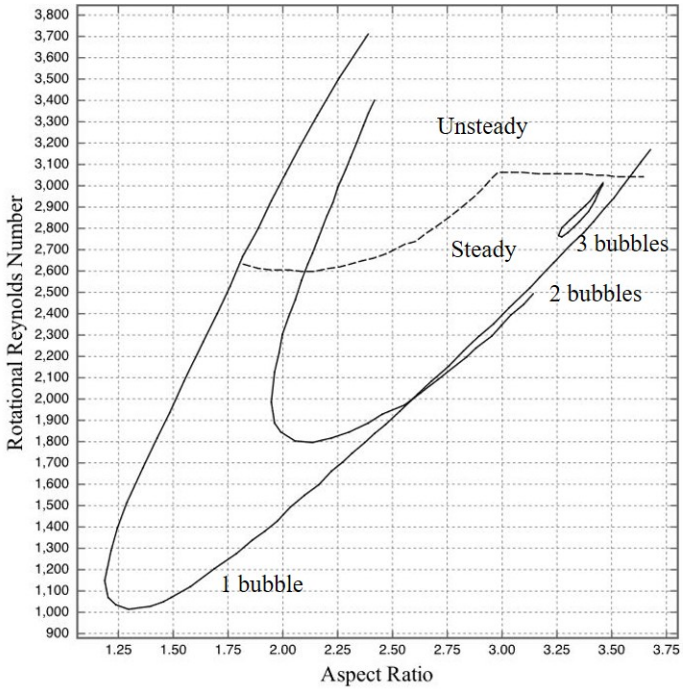

Figure 3.2: Parameter map of vortex breakdown for CC (reproduced from Escudier [19])

3.1.1 Axisymmetic incompressible flow simulation

Governing equations

Axisymmetric incompressible Navier-Stokes equations are written in cylindrical coordinates as

$$\partial_r u_r + \frac{u_r}{r} + \partial_z u_z = 0, \tag{3.2}$$

$$\partial_t u_r + u_r \partial_r u_r + u_z \partial_z u_r - \frac{u_\theta^2}{r} = -\partial_r p + \frac{1}{Re}(\partial_r^2 u_r + \frac{\partial_r u_r}{r} - \frac{u_r}{r^2} + \partial_z^2 u_r), \tag{3.3}$$

$$\partial_t u_\theta + u_r \partial_r u_\theta + u_z \partial_z u_\theta + \frac{u_r u_\theta}{r} = \frac{1}{Re}(\partial_r^2 u_\theta + \frac{\partial_r u_\theta}{r} - \frac{u_\theta}{r^2} + \partial_z^2 u_\theta), \tag{3.4}$$

$$\partial_t u_z + u_r \partial_r u_z + u_z \partial_z u_z = -\partial_z p + \frac{1}{Re}(\partial_r^2 u_z + \frac{\partial_r u_z}{r} + \partial_z^2 u_z). \tag{3.5}$$

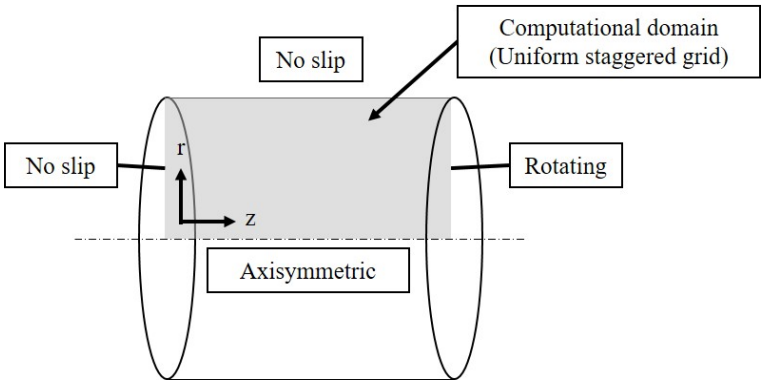

Figure 3.3: Computational domain and boundary conditions for *CC-Incomp*

Computational method

In this computation, the advection term is discretized by a 2nd-order consistent central difference scheme [33], and the other terms are discretized by a 2nd-order central difference scheme. To compute the above equations, SMAC method [16] is applied. This method is often used to simulate incompressible turbulent flows, as this procedure gives good convergence of the dilatation. It is a projection method: the flow data is at first predicted by calculating the governing equations and it is secondly modified by the pressure.

Computational condition

The computational domain and boundary conditions are schematically shown in Fig. 3.3. Boundary conditions are written in equations as

$$u_r(0,z) = 0, u_\theta(0,z) = 0, \partial_r u_z(0,z) = 0, \partial_r p(0,z) = 0, \tag{3.6}$$
$$u_r(r,0) = 0, u_\theta(r,0) = 0, u_z(r,0) = 0, \partial_z p(r,0) = 0, \tag{3.7}$$
$$u_r(1,z) = 0, u_\theta(1,z) = 0, u_z(1,z) = 0, \partial_r p(1,z) = 0, \tag{3.8}$$
$$u_r(r,H/R) = 0, u_\theta(r,H/R) = r, u_z(r,H/R) = 0, \partial_z p(r,H/R) = 0. \tag{3.9}$$

In this thesis, we simulate steady solutions at $\frac{H}{R} = 1.5$. Here, Re is variable:

$$1000 \leq Re \leq 1256 \tag{3.10}$$

The grid point is a uniform mesh and consists of 128 points in r-direction and 192 points in z-direction.

Validation

Table 3.1 shows the comparison of computational results with experimental reesults by Escudier [19] from an aspect of the position of stagnation points. The fine grid consists of 256 points in r-direction and 384 points in z-direction. The grid convergence was checked and no difference between normal and fine meshes was observed. As a result, we can see the computational results are in good agreement with the experimental results.

Table 3.1: Comparison of the position of stagnation points for *CC-Incomp*

Data type	Re	H/R	z_{up}	z_{down}
Experimental data [19]	1256	1.5	0.51	0.70
Numerical data (normal)	1256	1.5	0.51	0.71
Numerical data (fine)	1256	1.5	0.51	0.70

3.1.2 Axisymmetic low-Mach-number flow simulation

Governing equations

Majda and Sethian [40] derived axisymmetric low-Mach-number Navier-Stokes equations (LMN equations) by an order analysis of compressible Navier-Stokes equations in terms of a small perturbation, $\epsilon = \gamma M^2$. They are written in cylindrical coordinates as

$$\partial_t \rho + \partial_r(\rho u_r) + \frac{\rho u_r}{r} + \partial_z(\rho u_z) = 0, \tag{3.11}$$

$$\rho\partial_t u_r + \rho u_r \partial_r u_r + \rho u_z \partial_z u_r - \rho\frac{u_\theta^2}{r} = -\partial_r p_\epsilon + \frac{1}{Re}(\partial_r^2 u_r + \frac{\partial_r u_r}{r} - \frac{u_r}{r^2} + \partial_z^2 u_r), \tag{3.12}$$

$$\rho\partial_t u_\theta + \rho u_r \partial_r u_\theta + \rho u_z \partial_z u_\theta + \rho\frac{u_r u_\theta}{r} = \frac{1}{Re}(\partial_r^2 u_\theta + \frac{\partial_r u_\theta}{r} - \frac{u_\theta}{r^2} + \partial_z^2 u_\theta), \tag{3.13}$$

$$\rho\partial_t u_z + \rho u_r \partial_r u_z + \rho u_z \partial_z u_z = -\partial_z p_\epsilon + \frac{1}{Re}(\partial_r^2 u_z + \frac{\partial_r u_z}{r} + \partial_z^2 u_z), \tag{3.14}$$

$$\partial_r p = 0, \tag{3.15}$$

$$\partial_z p = 0, \tag{3.16}$$

$$p = \rho T. \tag{3.17}$$

We can see that the dissipation term through the viscosity vanishes because this term is smaller than the other terms by M^2 order. This is a typical feature of this LMN equations, and then, there is no variation of the entropy from the viscosity. Also, we can see two pressures, p and p_ϵ. p is uniform in the whole space and is conneted to the thermodynamical variables, while p_ϵ is a function in the space and is connected to the kinematic variables.

In this thesis, to be investigated by these equations is the compressibility effect on the bifurcation of the topology of the bubble-type vortex breakdown. The above equations are suited for the present purpose because there is no constraint on the topology. There exists the Boussinesq equations as another choice of LMN equations, but they assume the flow field satisfies the solenoidal condition [65]. It means the Boussinesq equations have a constraint on the topology of the flow field and is the main reason why they are not applied in this thesis.

Computational method

In this computation, the discretization method is same as that for *CC-Incomp* case. Nicoud [43] proposed a routine to solve the LMN equations, which we use in this thesis. At first, ρ ,T, and p are renewed because thermodynamical variables move faster than kinematic variables. Next, u_i and p_ϵ are renewed by the same method for *CC-Incomp* case.

Computational condition

We consider a fluid is the air. Table 3.2 shows reference values common to the all computations for *CC-LMN* case. The other parameter is the rotational speed of the disc. In this thesis, this parameter is calculated by the Reynolds number which we set.

Table 3.2: Reference values for *CC-LMN*

ρ_{ref}	T_{ref}	R_{ref}
$1.225[kg/m^3]$	$300[K]$	$0.1[m]$

Fig. 3.4 schematically shows the computational domain and boundary conditions. Boundary conditions are almost same as those for *CC-Incomp* case. The same parts are written in equations as

$$u_r(0,z)=0, u_\theta(0,z)=0, \partial_r u_z(0,z)=0, \partial_r p(0,z)=0, \tag{3.18}$$
$$u_r(r,0)=0, u_\theta(r,0)=0, u_z(r,0)=0, \partial_z p(r,0)=0, \tag{3.19}$$
$$u_r(1,z)=0, u_\theta(1,z)=0, u_z(1,z)=0, \partial_r p(1,z)=0, \tag{3.20}$$
$$u_r(r,H/R)=0, u_\theta(r,H/R)=r, u_z(r,H/R)=0, \partial_z p(r,H/R)=0. \tag{3.21}$$

Only the difference is the existence of the boundary condition for T. From the simulation of the LMN equations, we investigate the additional bifurcation of the topology for an unsteady compressible flow. Then, in order to obtain such a solution, at the static wall with the variable temperature, the boundary condition for T is set as

$$T(r,0)=1+\Delta T\cos\frac{2\pi t}{\Omega_f}, \tag{3.22}$$

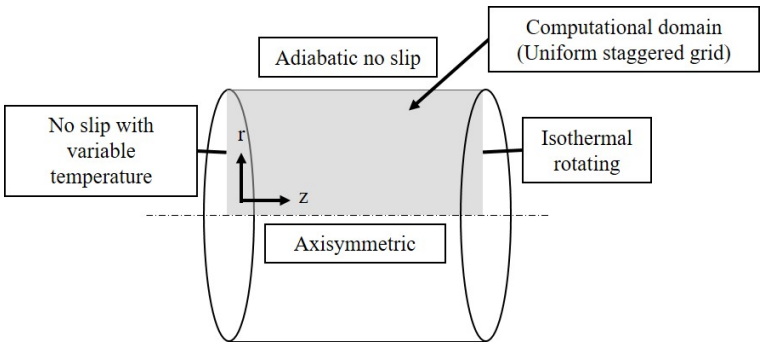

Figure 3.4: Computational domain and boundary conditions for *CC-LMN*

where ΔT is the difference in temperature, and Ω_f is the frequency of the temperature variation. At the other boundaries,

$$\partial_r T(0,z) = 0, \partial_r T(1,z) = 0, T(r, H/R) = 1. \tag{3.23}$$

In this thesis, we simulate unsteady (periodic) solutions for $Re = 1100, 1400$ at $H/R = 2.0$. Table 3.3 summarizes the setting of the parameters. The grid point is a uniform mesh and consists of 128 points in r-direction and 256 points in z-direction.

Table 3.3: Area of investigation for *CC-LMN*

Re	H/R	Pr	ΔT	Ω_f
1100	2	0.7	0.2	100
1400	2	0.7	0.1	100

Validation

In oreder to validate the computational results, a steady solution is numerically simulated for $(Re, H/R, \Delta T) = (1256, 1.5, 0)$. Table 3.4 shows the comparison of the position of stagnation points among the computational result for *CC-LMN* case, the computational result for *CC-Incomp*, and the experimental result by Escudier [19].

3.2 Flow in swirling jet with free-slip boundaries

Fundamental studies on vortex breakdown have been conducted not only in a close cylinder but also in a divergent pipe. Harvey showed that a vortex breakdown took place in a divergent pipe whose

Table 3.4: Comparison of the position of stagnation points for *CC-LMN*

Data type	Re	$\frac{H}{R}$	z_{up}	z_{down}
Experimental data [19]	1256	1.5	0.51	0.70
Numerical data (*CC-Incomp*)	1256	1.5	0.51	0.71
Numerical data (*CC-LMN*)	1256	1.5	0.51	0.71

inlet has swirling vanes like a rotary compressor [29]. Sarpkaya comprehensively investigated the vortex breakdown in the divergent pipe and he observed several types of the vortex breakdowns: bubble-type, spiral-type, double-helix-type [54], and turbulent vortex breakdowns [55].

As there were lots of experimental results, numerical simulations of a swiring flow in a pipe were attempted but it was quite sensitive to boundary conditions especially at the inlet and the outlet [9]. Then, Grabowski and Steger computed an axisymmetric swirling flow with free-slip boundaries [26]. They numerically produced a bubble-type vortex breakdown whose shape was similar to the experimental one. They imposed an exact solution of Euler equations such that

$$u_r = 0, \tag{3.24}$$

$$u_z = \begin{cases} \alpha + (1-\alpha)r^2(6-8r+3r^2) & (r<1) \\ 1 & (otherwise) \end{cases} \tag{3.25}$$

$$u_\theta = \begin{cases} Sr(2-r^2), & (r<1) \\ \frac{S}{r}, & (otherwise) \end{cases} \tag{3.26}$$

where S is a swirling parameter and α is an axial parameter: The axial velocity is jet-like if $\alpha > 1$ and wake-like if $\alpha < 1$. This profile was investigated in a fully three-dimensional flow by Ruith *et al.* [52]. They found not only a bubble-type vortex breakdown but also a spiral-type and a double-helix-type vortex breakdowns. Also, they found the transition from the steady bubble-type vortex breakdown to the periodic spiral-type vortex breakdown. Then, their result indicated that the stability breaking caused the transition to the spiral-type vortex breakdown.

This scinario was confirmed by a stability analysis as shown in Chapter 1. However, the stability analyses in previous studies were based on an axisymmetric bubble-type vortex breakdown, because only an axisymmetric steady solution was obtained from the Grabowski profile.

In this thesis, we modify the Grabowski profile in order to investigate assymetric bubble-type vortex breakdowns. After showing the governing equations, we introduce another velocity profile called *misaligned Grabowski profile*. This profile satisfies the Euler equation as well as the original profile and enables us to yield a fully three-dimensional bubble-type vortex breadown as a base flow.

3.2.1 Fully three-dimensional compressible flow simulation

Governing equations

Compressible Navier-Stokes equations in Cartesian coordinates are written as

$$\partial_t \rho + \partial_x m_x + \partial_y m_y + \partial_z m_z = 0, \tag{3.27}$$
$$\partial_t m_x + \partial_x (m_x u_x) + \partial_y (m_x u_y) + \partial_z (m_x u_z) = -\partial_x p + \partial_x \tau_{xx} + \partial_y \tau_{xy} + \partial_z \tau_{xz}, \tag{3.28}$$
$$\partial_t m_y + \partial_x (m_y u_x) + \partial_y (m_y u_y) + \partial_z (m_y u_z) = -\partial_y p + \partial_x \tau_{yx} + \partial_y \tau_{yy} + \partial_z \tau_{yz}, \tag{3.29}$$
$$\partial_t m_z + \partial_x (m_z u_x) + \partial_y (m_z u_y) + \partial_z (m_z u_z) = -\partial_z p + \partial_x \tau_{zx} + \partial_y \tau_{zy} + \partial_z \tau_{zz}, \tag{3.30}$$
$$\partial_t (\rho E) + \partial_x [(\rho E + p) u_x] + \partial_y [(\rho E + p) u_y] + \partial_z [(\rho E + p) u_z] \tag{3.31}$$
$$= \partial_x (u_x \tau_{xx} + u_y \tau_{yx} + u_z \tau_{zx} + q_x) + \partial_y (u_x \tau_{xy} + u_y \tau_{yy} + u_z \tau_{zy} + q_y) + \partial_z (u_x \tau_{xz} + u_y \tau_{yz} + u_z \tau_{zz} + q_z),$$

where $m_i (i = x, y, z)$ are momentum flux components in Cartesian coordinates, E is a total energy per mass, $\tau_{ij} (i = x, y, z, j = x, y, z)$ are elements of a viscous stress tensor, and $q_i (i = x, y, z)$ are heat flux components. They are written as

$$m_i \equiv \rho u_i, \tag{3.32}$$
$$E \equiv \frac{1}{\gamma - 1} \frac{p}{\rho} + \frac{1}{2} (u_x^2 + u_y^2 + u_z^2), \tag{3.33}$$
$$\tau_{ij} \equiv \mu [\partial_i u_j + \partial_j u_i - \frac{2}{3} \delta_{ij} (\partial_x u_x + \partial_y u_y + \partial_z u_z)], \tag{3.34}$$
$$q_i \equiv \frac{\mu}{(\gamma - 1) Re Pr M^2} \partial_i T, \tag{3.35}$$

where μ is the kinematic viscosity of the fluid calculated by Sutherland equation:

$$\mu = C_1 \frac{T^{\frac{3}{2}}}{T + C_2}, \tag{3.36}$$

where T is temperature.

Computational method

These equations are discretized by the 6th-order compact scheme [36], in which the 2nd-order one-sided and the 4th-order central difference schemes are used at the edge point and the second one from it respectively. Also, in order to remove numerical high-frequency oscillation, 10th-order low pass filter is used. The discretized equations are integrated in time, t, by the 3rd-order TVD-Runge-Kutta method.

Computational condition

We consider a fluid is the air as well as *CC-LMN* case. Table 3.5 shows reference values common to the all computations for *SJ-Comp* case. In this case, the characteristic length is calculated by the Reynolds number and the Mach number which we set.

Table 3.5: Reference values for *SJ-Comp*

ρ_{ref}	T_{ref}
$1.225[kg/m^3]$	$300[K]$

We can obtain the misaligned Grabowski profile by adding an offset parameter to the Grabowski profile. The misaligned Grabowski profile is written as

$$u_r = 0, \tag{3.37}$$

$$u_z = \begin{cases} \alpha + (1-\alpha) r_{off}^2 (6 - 8 r_{off} + 3 r_{off}^2) & (r_{off} < 1) \\ 1 & (otherwise) \end{cases} \tag{3.38}$$

$$u_\theta = \begin{cases} Sr(2 - r^2), & (r < 1) \\ \frac{S}{r}, & (otherwise) \end{cases} \tag{3.39}$$

where r_{off} is the offset parameter defined as

$$r_{off} = \sqrt{x_{off}^2 + y_{off}^2}. \tag{3.40}$$

Fig. 3.5 shows the contour map of the axial velocity with white vectors of the rotational velocity of both profiles. We can see there exists the offset between the center axis of the jet-like axial velocity and the center axis of the swirling velocity. It satisfies the solenoidal condition of the velocity vector field and is also an exact solution of Euler equations.

There are some paramters we can control. In this thesis, Re, M, and α are fixed:

$$Re = 200, \tag{3.41}$$

$$M = 0.2, \tag{3.42}$$

$$\alpha = 1.2. \tag{3.43}$$

The others are variable parameters:

$$0.9 \leq S \leq 1.0, \tag{3.44}$$

$$0 \leq r_{off} \leq 0.5. \tag{3.45}$$

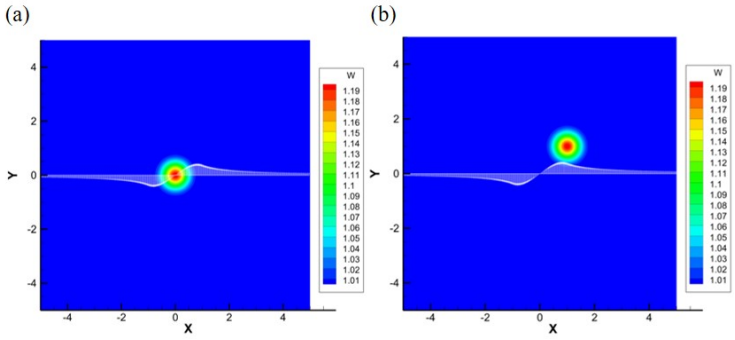

Figure 3.5: Contour map of the axial velocity with vectors of the rotational velocity: (a) Grabowski profile (b) misaligned Grabowski profile for $(x_{off}, y_{off}) = (1, 1)$

Fig. 3.6 shows the area of investigations in this thesis.

At this area, it is known that a periodic spiral-type vortex breakdown takes place for an incompressible flow [52]. We need to obtain an unstable steady solution for a global stability analysis. Then, the unstable steady solution is calculated by the SFD method introduced in Chapter 2.

Fig. 3.7 shows the computational domain and boundary conditions. In order to avoid non-physical reflections of propagating waves at boundaries, we often apply characteristic boundary conditions. Here, the boundary conditions at the inlet and the outlet are Navier-Stokes characterstic boundary conditions (NSCBC) for subsonic inflow and outflow proposed by Ponsiot and Lele [48], respectively. The NSCBC is based on a simple characteristic boundary condition (CBC) using local one-dimensional inviscid (LODI) relations proposed by Thompson [61]. For example, when we consider the normal condition to the boundary is x, a LODI system can be written as

$$\partial_t \begin{pmatrix} \rho \\ u_x \\ u_y \\ u_z \\ p \end{pmatrix} + \begin{pmatrix} u_x & \rho & 0 & 0 & 0 \\ 0 & u_x & 0 & 0 & \frac{1}{\rho} \\ 0 & 0 & u_x & 0 & 0 \\ 0 & 0 & 0 & u_x & 0 \\ 0 & \gamma p & 0 & 0 & u_x \end{pmatrix} \partial_x \begin{pmatrix} \rho \\ u_x \\ u_y \\ u_z \\ p \end{pmatrix} = \begin{pmatrix} 0 \\ 0 \\ 0 \\ 0 \\ 0 \end{pmatrix}. \tag{3.46}$$

We can rewrite this system to

$$\partial_t \begin{pmatrix} p - \rho c u_x \\ c^2\rho - p \\ u_y \\ u_z \\ p + \rho c u_x \end{pmatrix} + \begin{pmatrix} u_x - c & \rho & 0 & 0 & 0 \\ 0 & u_x & 0 & 0 & 0 \\ 0 & 0 & u_x & 0 & 0 \\ 0 & 0 & 0 & u_x & 0 \\ 0 & 0 & 0 & 0 & u_x + c \end{pmatrix} \partial_x \begin{pmatrix} p - \rho c u_x \\ c^2\rho - p \\ u_y \\ u_z \\ p + \rho c u_x \end{pmatrix} = \begin{pmatrix} 0 \\ 0 \\ 0 \\ 0 \\ 0 \end{pmatrix}, \tag{3.47}$$

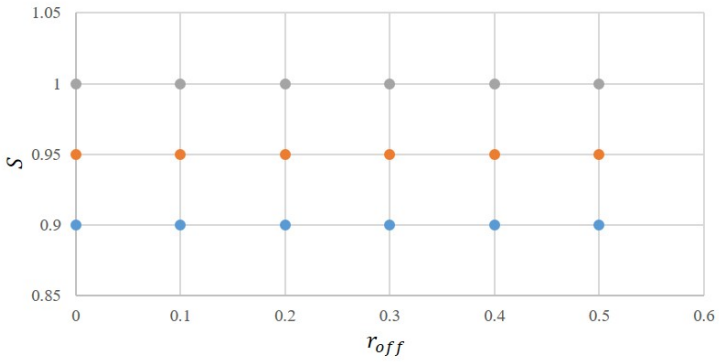

Figure 3.6: Area of investigations for *SJ-Comp*

where c is a sonic speed written as

$$c = \sqrt{\frac{\gamma p}{\rho}}. \tag{3.48}$$

For a subsonic flow, there are four incomig waves from the outside of the computational domain at the inlet, while there is only one incoming waves at the outlet. Giving some variables at the boundary, we can calculate the other variables by the LODI system without the numerical oscillation. This is the procedure of the characteristic boundary condition by Thomson [61]. On the NSCBC, we calculate Navier-Stoke equations again using differential terms in x-direction obtained from the LODI system.

The other boundary conditions are isothermal free-slip boundaries written as

$$T = 1, \tag{3.49}$$
$$u_n = 0, \tag{3.50}$$
$$\tau_{nj} = 0, \tag{3.51}$$

where n is the normal direction. The misaligned Grabowski profile is set as the initial condition of the computation, and then, the numerical solution at the next step is calculated. The grid point consists of 160 points in both x-direction and y-direction, and 192 points in z-direction.

Validation

In this configuration, we do not have experimental results to compare but computational results for incompressible flows. Here, a computational result for $(Re, M, \alpha, S, r_{off}) = (200, 0.2, 1, 1, 0)$

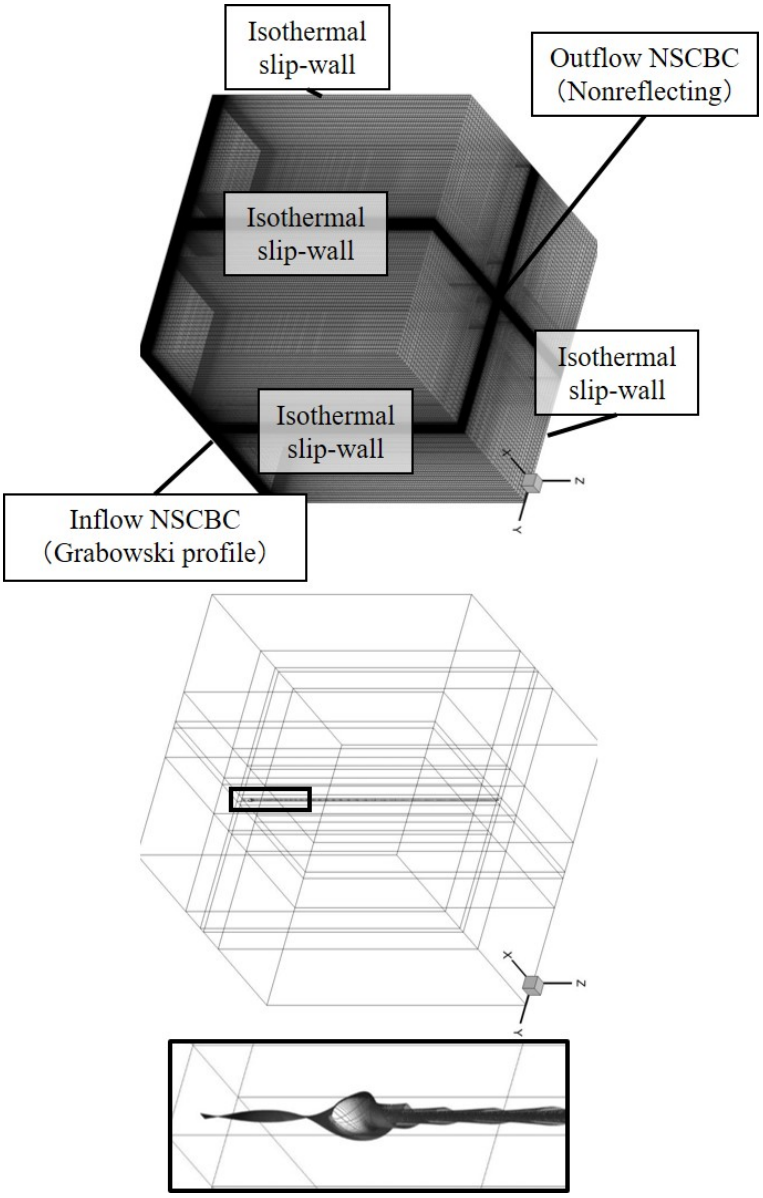

Figure 3.7: Computational grid with boundary conditions, computational domain with streamlines, and zoomed-in view of streamlines for *SJ-Comp*

is compared to the computational result by Qadri *et al.* [49] from an aspect of the locations of stagnation points. Table 3.6 shows the comparison between the present result and the reference result. The fine mesh consists of 240 points in both x-direction and $y$direction, and 288 points in z-direction. We can see the present result is in good agreement with the result of Qadri *et al.* [49] by 2% about the locations of stagnation points.

Table 3.6: Comparison of the position of stagnation points for *SJ-Comp*

Data type	Re	α	S	z_{up}	z_{down}
Numerical data (incompressible) [49]	200	1	1	1.32	2.21
Numerical data (normal)	200	1	1	1.31	2.18
Numerical data (fine)	200	1	1	1.30	2.18

3.2.2 Linearized Navier-Stokes equations

Governing equations

In this thesis, we analyze a global stability on not only linearized Navier-Stokes equations but also adjoint Navier-Stokes equations. In order to derive the adjoint equations, it is convinient to use the pressure instead of the total energy. The pressure equation can be written as

$$\begin{aligned}&\partial_t p + \partial_x(pu_x) + \partial_y(pu_y) + \partial_z(pu_z) \\ &= (\gamma-1)[-p(\partial_x u_x + \partial_y u_y + \partial_z u_z) + \partial_x q_x + \partial_y q_y + \partial_z q_z \\ &+\tau_{xx}\partial_x u_x + \tau_{yy}\partial_y u_y + \tau_{zz}\partial_z u_z + \tau_{xy}(\partial_y u_x + \partial_x u_y) + \tau_{yz}(\partial_z u_y + \partial_y u_z) + \tau_{zx}(\partial_x u_z + \partial_z u_x)].\end{aligned} \tag{3.52}$$

We can write the linearized Navier-Stokes equations for fully three-dimensional compressible flows as follows:

$$\partial_t \rho' + \partial_x m_x^{'} + \partial_y m_y^{'} + \partial_z m_z^{'} = 0, \tag{3.53}$$

$$\partial_t m_x^{'} + \partial_x(m_x^{'} u_x) + \partial_y(m_x^{'} u_y) + \partial_z(m_x^{'} u_z) + \partial_x(m_x u_x^{'}) + \partial_y(m_x u_y^{'}) + \partial_z(m_x u_z^{'}) \tag{3.54}$$
$$= -\partial_x p^{'} + \partial_x \tau_{xx}^{'} + \partial_y \tau_{xy}^{'} + \partial_z \tau_{xz}^{'},$$

$$\partial_t m_y^{'} + \partial_x(m_y^{'} u_x) + \partial_y(m_y^{'} u_y) + \partial_z(m_y^{'} u_z) + \partial_x(m_y u_x^{'}) + \partial_y(m_y u_y^{'}) + \partial_z(m_y u_z^{'}) \tag{3.55}$$
$$= -\partial_y p^{'} + \partial_x \tau_{yx}^{'} + \partial_y \tau_{yy}^{'} + \partial_z \tau_{yz}^{'},$$

$$\partial_t m_z^{'} + \partial_x(m_z^{'} u_x) + \partial_y(m_z^{'} u_y) + \partial_z(m_z^{'} u_z) + \partial_x(m_z u_x^{'}) + \partial_y(m_z u_y^{'}) + \partial_z(m_z u_z^{'}) \tag{3.56}$$
$$= -\partial_z p^{'} + \partial_x \tau_{zx}^{'} + \partial_y \tau_{zy}^{'} + \partial_z \tau_{zz}^{'},$$

$$\partial_t p^{'} + \partial_x(p^{'} u_x) + \partial_y(p^{'} u_y) + \partial_z(p^{'} u_z) + \partial_x(p u_x^{'}) + \partial_y(p u_y^{'}) + \partial_z(p u_z^{'}) \tag{3.57}$$
$$= (\gamma - 1)[-p'(\partial_x u_x + \partial_y u_y + \partial_z u_z) - p(\partial_x u_x^{'} + \partial_y u_y^{'} + \partial_z u_z^{'}) + \partial_x q_x^{'} + \partial_y q_y^{'} + \partial_z q_z^{'}$$
$$+\partial_x u_x^{'} \tau_{xx} + \partial_y u_y^{'} \tau_{yy} + \partial_z u_z^{'} \tau_{zz} + (\partial_x u_y^{'} + \partial_y u_x^{'})\tau_{xy} + (\partial_y u_z^{'} + \partial_z u_y^{'})\tau_{yz} + (\partial_z u_x^{'} + \partial_x u_z^{'})\tau_{zx}$$
$$+\partial_x u_x \tau_{xx}^{'} + \partial_y u_y \tau_{yy}^{'} + \partial_z u_z \tau_{zz}^{'} + (\partial_x u_y + \partial_y u_x)\tau_{xy}^{'} + (\partial_y u_z + \partial_z u_y)\tau_{yz}^{'} + (\partial_z u_x + \partial_x u_z)\tau_{zx}^{'}],$$

where $m_i^{'}(i = x, y, z)$ are momentum flux perturbations in Cartesian coordinates, $\tau_{ij}^{'}(i = x, y, z, j = x, y, z)$ are elements of a perturbed viscous stress tensor, and $q_i^{'}(i = x, y, z)$ are heat flux perturbations. They are written as

$$m_i^{'} \equiv \rho' u_i + \rho u_i^{'}, \tag{3.58}$$

$$\tau_{ij}^{'} \equiv \mu[\partial_i u_j^{'} + \partial_j u_i^{'} - \frac{2}{3}\delta_{ij}(\partial_x u_x^{'} + \partial_y u_y^{'} + \partial_z u_z^{'})] \tag{3.59}$$
$$+ \mu'[\partial_i u_j + \partial_j u_i - \frac{2}{3}\delta_{ij}(\partial_x u_x + \partial_y u_y + \partial_z u_z)],$$

$$q_i^{'} \equiv \frac{\mu}{(\gamma - 1)RePrM^2}\partial_i T' + \frac{\mu'}{(\gamma - 1)RePrM^2}\partial_i T, \tag{3.60}$$

where μ is the perturbation of the kinematic viscosity obtained by differentiating the Sutherland equation in T:

$$\mu' \equiv \frac{d\mu}{dT}T' = C_1(\frac{3}{2}\frac{T^{\frac{1}{2}}}{T + C_2} - \frac{T^{\frac{3}{2}}}{(T + C_2)^2})T', \tag{3.61}$$

where T' is temperature perturbation.

Computational method

The linearized equations are solved by the same way as the compressible Navier-Stokes equations.

Computational condition

we need to solve the linealized Navier-Stokes equations for the global stability analysis, because the time-stepping method is used. The computational domain is the same as the domain for the nonlinear Navier-Stokes equations but boundary conditions are slightly different as shown in Fig. 3.8. Instead of the characteristic boundary conditions at the inlet and the outlet, charcteristic boundary conditions [61] are simply imposed there. For example, when we consider the normal condition to the boundary is x, the LODI system can be written as

$$\partial_t \begin{pmatrix} \rho' \\ u_x' \\ u_y' \\ u_z' \\ p' \end{pmatrix} + \begin{pmatrix} u_x & \rho & 0 & 0 & 0 \\ 0 & u_x & 0 & 0 & \frac{1}{\rho} \\ 0 & 0 & u_x & 0 & 0 \\ 0 & 0 & 0 & u_x & 0 \\ 0 & \gamma p & 0 & 0 & u_x \end{pmatrix} \partial_x \begin{pmatrix} \rho' \\ u_x' \\ u_y' \\ u_z' \\ p' \end{pmatrix} = \begin{pmatrix} 0 \\ 0 \\ 0 \\ 0 \\ 0 \end{pmatrix}. \tag{3.62}$$

At the inlet, there are four incoming waves which should be estimated, while there is only one incoming wave at the outlet. Then, $\rho' = 0$ and $\mathbf{m}' = \mathbf{0}$ are imposed at the inlet, and $p' = 0$ is imposed at the outlet.

On the other boundaries, the isothermal free-slip conditions are imposed. We can write the isothermal free-slip boundary as

$$T' = 0, \tag{3.63}$$
$$u_n' = 0, \tag{3.64}$$
$$\tau_{nj}' = 0, \tag{3.65}$$

where n is the normal direction.

3.2.3 Adjoint Navier-Stokes equations

Governing equations

When we derive adjoint Naveir-Stokes equations, we need to integrate the linearized Navier-Stokes equation by parts. The manipulation is written in Appendix B because it is long and comlicated.

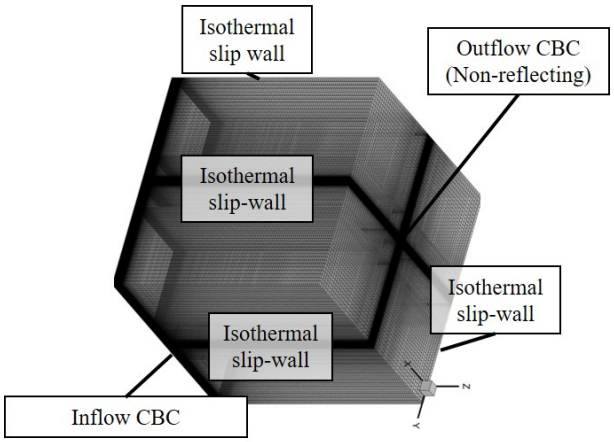

Figure 3.8: Computational grid and boundary conditions for linearized Navier-Stokes equations

Here, we see only the adjoint Navier-Stokes equations written as

$$\partial_t \rho^* + \frac{p}{\rho}(u_x \partial_x \rho^* + \partial_y \rho^* + \partial_z \rho^*) + (\gamma - 1)\frac{p^*}{\rho}(u_x \partial_x p + \partial_y p + \partial_z p) \tag{3.66}$$
$$= -u_x(u_x \partial_x m_x^* + \partial_y m_x^* + \partial_z m_x^*) - u_y(u_x \partial_x m_y^* + \partial_y m_y^* + \partial_z m_y^*) - u_z(u_x \partial_x m_z^* + \partial_y m_z^* + \partial_z m_z^*)$$
$$+\frac{1}{\rho}[\partial_x(u_x \sigma_{xx} + u_y \sigma_{yx} + u_z \sigma_{zx}) + \partial_y(u_x \sigma_{xy} + u_y \sigma_{yy} + u_z \sigma_{zy}) + \partial_z(u_x \sigma_{xz} + u_y \sigma_{yz} + u_z \sigma_{zz})]$$
$$-\frac{p}{\rho}(s_{visc}^* + s_{heat}^*),$$
$$\partial_t m_x^* - u_x \partial_x m_x^* - u_y \partial_y m_x^* - u_z \partial_z m_x^* + u_x \partial_x m_x^* + u_y \partial_x m_y^* + u_z \partial_x m_z^* \tag{3.67}$$
$$= \partial_x \rho^* + \gamma \frac{p}{\rho} \partial_x p^* + \frac{1}{\rho}(\partial_x \sigma_{xx}^* + \partial_y \sigma_{xy}^* + \partial_z \sigma_{xz}^*),$$
$$\partial_t m_y^* - u_x \partial_x m_y^* - u_y \partial_y m_y^* - u_z \partial_z m_y^* + u_x \partial_y m_x^* + u_y \partial_y m_y^* + u_z \partial_y m_z^* \tag{3.68}$$
$$= \partial_y \rho^* + \gamma \frac{p}{\rho} \partial_y p^* + \frac{1}{\rho}(\partial_x \sigma_{yx}^* + \partial_y \sigma_{yy}^* + \partial_z \sigma_{yz}^*),$$
$$\partial_t m_z^* - u_x \partial_x m_z^* - u_y \partial_y m_z^* - u_z \partial_z m_z^* + u_x \partial_z m_x^* + u_y \partial_z m_y^* + u_z \partial m_z^* \tag{3.69}$$
$$= \partial_z \rho^* + \gamma \frac{p}{\rho} \partial_z p^* + \frac{1}{\rho}(\partial_x \sigma_{zx}^* + \partial_y \sigma_{zy}^* + \partial_z \sigma_{zz}^*),$$
$$\partial_t p^* - \partial_x m_x^* - \partial_y m_y^* - \partial_z m_z^* \tag{3.70}$$
$$= u_x \partial_x p^* + u_y \partial_y p^* + u_z \partial_z p^* - (\gamma - 1)(\partial_x u_x + \partial_y u_y + \partial_z u_z) p^*$$
$$+s_{visc}^* + s_{heat}^*,$$

where $m_i^*(i = x, y, z)$ are adjoint momentum fluxes in Cartesian coordinates, $\sigma_{ij}^*(i = x, y, z, j = x, y, z)$ are elements of an adjoint viscous stress tensor, and s_{visc}^*, s_{heat}^* are source terms from the viscosity and the heat. They are written as

$$m_i^* \equiv \rho^* u_i + \rho u_i^*, \tag{3.71}$$

$$\sigma_{ij}^* \equiv \tau_{ij}^* - 2(\gamma - 1)\tau_{ij}\rho^*, \tag{3.72}$$

$$\tau_{ij}^* \equiv \mu[\partial_i m_j^* + \partial_j m_i^* - \frac{2}{3}\delta_{ij}(\partial_x m_x^* + \partial_y m_y^* + \partial_z m_z^*)] \tag{3.73}$$

$$\begin{aligned} s_{visc}^* \equiv & -\frac{T}{p}\frac{d\mu}{dT} \\ & \{[\partial_x m_x^* - (\gamma-1)\partial_x u_x p^*]\frac{\tau_{xx}}{\mu} + [\partial_x m_y^* - (\gamma-1)\partial_x u_y p^*]\frac{\tau_{xy}}{\mu} + [\partial_x m_z^* - (\gamma-1)\partial_x u_z p^*]\frac{\tau_{xz}}{\mu} \\ & + [\partial_y m_x^* - (\gamma-1)\partial_y u_x p^*]\frac{\tau_{yx}}{\mu} + [\partial_y m_y^* - (\gamma-1)\partial_y u_y p^*]\frac{\tau_{yy}}{\mu} + [\partial_y m_z^* - (\gamma-1)\partial_y u_z p^*]\frac{\tau_{yz}}{\mu} \\ & + [\partial_z m_x^* - (\gamma-1)\partial_z u_x p^*]\frac{\tau_{zx}}{\mu} + [\partial_z m_y^* - (\gamma-1)\partial_z u_y p^*]\frac{\tau_{zy}}{\mu} + [\partial_z m_z^* - (\gamma-1)\partial_z u_z p^*]\frac{\tau_{zz}}{\mu}\}, \end{aligned} \tag{3.74}$$

$$s_{heat}^* \equiv \frac{\gamma}{\rho Pr Re}[\partial_x(\mu\partial_x p^*) + \partial_y(\mu\partial_y p^*) + \partial_z(\mu\partial_z p^*) - \frac{d\mu}{dT}(\partial_x T\partial_x p^* + \partial_y T\partial_y p^* + \partial_z T\partial_z p^*). \tag{3.75}$$

Computational method

The adjoint equations are solved by the same way as the set of the compressible Navier-Stokes equations.

Computational condition

With the adjoint equations obtained through an integral by part, we obtain a boundary term also. It is written as

$$b = b_{Euler} + b_{visc} + b_{heat} \tag{3.76}$$

$$b_{Euler} = \int_{\partial\Omega}[\rho^* m_i^{'} + p' m_i^* + m_j^*(m_i^{'} u_j + m_i u_j^{'}) + p^*(p' u_i + \gamma p u_i^{'})]dA_i \tag{3.77}$$

$$b_{visc} = \int_{\partial\Omega}[\tau_{ij}^{'} m_j^* - \tau_{ij}^* u_j^{'} + 2(\gamma-1)p^*\tau_{ij}u_j^{'}]dA_i \tag{3.78}$$

$$b_{heat} = \int_{\partial\Omega}[(\gamma-1)p^* q_i^{'} - \partial_i p^* \frac{\mu}{M^2 Re Pr}T']dA_i. \tag{3.79}$$

We also need to solve the adjoint Navier-Stokes equations for the global stability analysis, because the time-stepping method is used. Then, we need to impose boundary conditions on boundaries but

we must be careful for the boundary conditions for the adjoint equations because of the existence of the boundary term.

Substituting (direct) boundary conditions for the linearized Navier-Stokes equations to the boundary term, we can choose the adjoint boundary conditions to get $b = 0$. It is known that, if the direct boundary condition is an inflow (outflow) characteristic boundary condition, the adjoint boundary condition becomes an outflow (inflow) characteristic boundary condition [25]. Fig. 3.9 shows the computational domain and the adjoint boundary conditions. Note that the boundary conditions at the inlet and the outlet are outflow and inflow characteristic boundary conditions, respectively.

When we consider the normal condition to the boundary is x, the adjoint LODI system can be written as

$$\partial_t \begin{pmatrix} \rho^* \\ u_x^* \\ u_y^* \\ u_z^* \\ p^* \end{pmatrix} - \begin{pmatrix} 0 & -\rho u_x^2 & 0 & 0 & -u(c^2+u^2) \\ \frac{1}{\rho} & u_x & 0 & 0 & \frac{c^2}{\rho} \\ 0 & 0 & u_x & 0 & 0 \\ 0 & 0 & 0 & u_x & 0 \\ 0 & \rho & 0 & 0 & 2u_x \end{pmatrix} \partial_x \begin{pmatrix} \rho^* \\ u_x^* \\ u_y^* \\ u_z^* \\ p^* \end{pmatrix} = \begin{pmatrix} 0 \\ 0 \\ 0 \\ 0 \\ 0 \end{pmatrix}. \tag{3.80}$$

In contrast to the direct boundary conditions, at the inlet, there is only one incoming wave, while there are four incoming waves at the outlet. Then, $\rho^* = 0$ and $\mathbf{m}^* = \mathbf{0}$ are imposed at the outlet, and $p^* = 0$ is imposed at the inlet.

We can also write the adjoint isothermal free-slip boundary as

$$p^* = 0, \tag{3.81}$$
$$u_n^* = 0, \tag{3.82}$$
$$\tau_{nj}^* = 0, \tag{3.83}$$

where n is the normal direction.

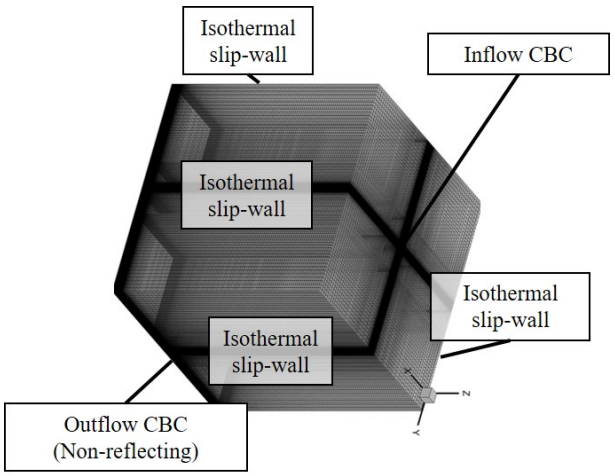

Figure 3.9: Computational domain and boundary conditions for adjoint Navier-Stokes equations

Chapter 4

Local Bifurcation Analysis on Bubble-Type Vortex Breakdown

In this chapter, results of topological analyses are shown and discussed. Beggining from the results for *CC-Incomp* case, we see the results for *CC-LMN* case and for *SJ-Comp* case, respectively. The topological analyses consist of the eigenvalue analysis of a velocity gradient tensor at a stagnation point for all the cases and the bifurcation analysis of the streamline topology for the axisymmetric cases. As shown in Chpater 1, the eigenvalue analysis of the velocity gradient tensor is the most fundamental structure of a dynamical system of streamlines and it is known that the stagnation point is a saddle-focus [66]. It is shown that this topological structure of the stagnation point is identical for the all cases even if the recirculating flow region is asymmetric or the flow includes the compressibility. Moreover, we see that there exists only one stagnation point at the onset of the bubble-type vortex breakdown and it is non-hyperbolic for *CC-Incomp* case. Next, introducing a two-parameter bifurcation model for the bifurcation of the topology of instantaneous streamlines for compressible flows, other topologies, which have not been observed in literature of flow simulations or experiments but mathematically predicted by Guckenheimer and Holmes [27], are found in instantaneous streamlines for *CC-LMN* case. Finally, we see and examine the axisymmetry breaking of the streamline topology of the bubble-type vortex breakdown for *SJ-Comp* case. Fig. 4.1 shows the research table and what is investigated in Chapter 4.

4.1 Axisymmetric incompressible case

4.1.1 Eigenanalysis of velocity gradient tensor

In this section, we revisit the identification of the topological structure of stagnation-point pairs. Aformentioned in Chapter 1, the saddle focus structure of the stagnation point is the most fun-

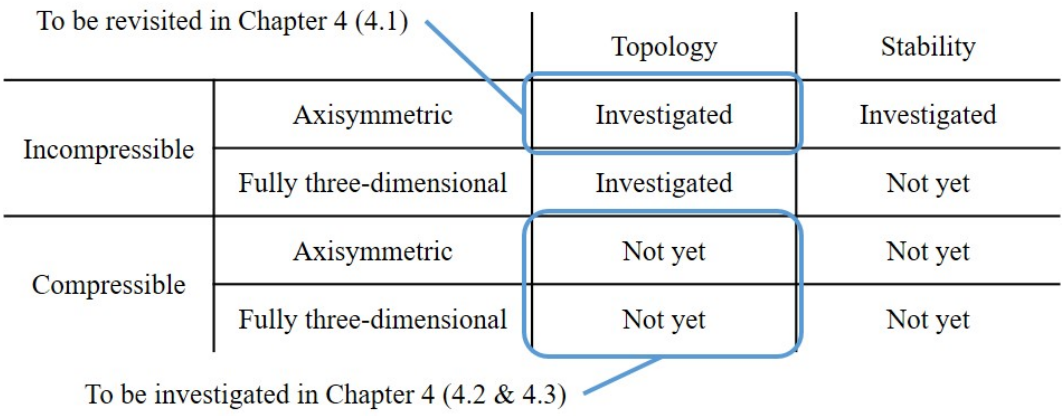

Figure 4.1: Research table and what is investigated in Chapter 4

damental property of the vortex breakdown. Results shown in this section are based on the preliminary investigation for *CC-Incomp* case by the authors [72].

Here, we see both *stagnation points* and *fixed points*. The stagnation point is used for a stationary point in a three-dimensional flow field and the fixed point is used for a stationary point in a space we choose. Then, stagnation points are fixed points but not vice versa. Fig. 4.2 shows a computed flow field for $Re = 1256$. Rotating the wall at $z = 1.5$, we have a counter-clockwise circulating flow. In some regions of the Reynolds number, we can observe a recirculating flow region along the axis. It is a buble-type vortex breakdown in the closed cylinder. In rz-plane, there are three fixed points. One is a fixed point off the axis, then it is a periodic orbit in xyz-plane. The others are the pair of stagnation points.

We see the velocity gradient tensors of stagnation points in xyz-plane. How to construct the velocity gradient tensor is rewritten here. At first, we look for the stagnation point from CFD data. It is represented by a grid point where the velocity is the lowest. Next, differentials of the velocity components are calculated by the 2nd central difference method.

For *CC-Incomp* case, the velocity gradient tensor and its eigenvalues at both stagnation points upstream and downstream of the recirculating flow region for $Re = 1256$ are

$$A_{up} = \begin{pmatrix} 0.062 & -0.056 & 0 \\ 0.056 & 0.062 & 0 \\ 0 & 0 & -0.124 \end{pmatrix}, \tag{4.1}$$

$$A_{down} = \begin{pmatrix} -0.030 & -0.096 & 0 \\ 0.096 & -0.030 & 0 \\ 0 & 0 & 0.060 \end{pmatrix}, \tag{4.2}$$

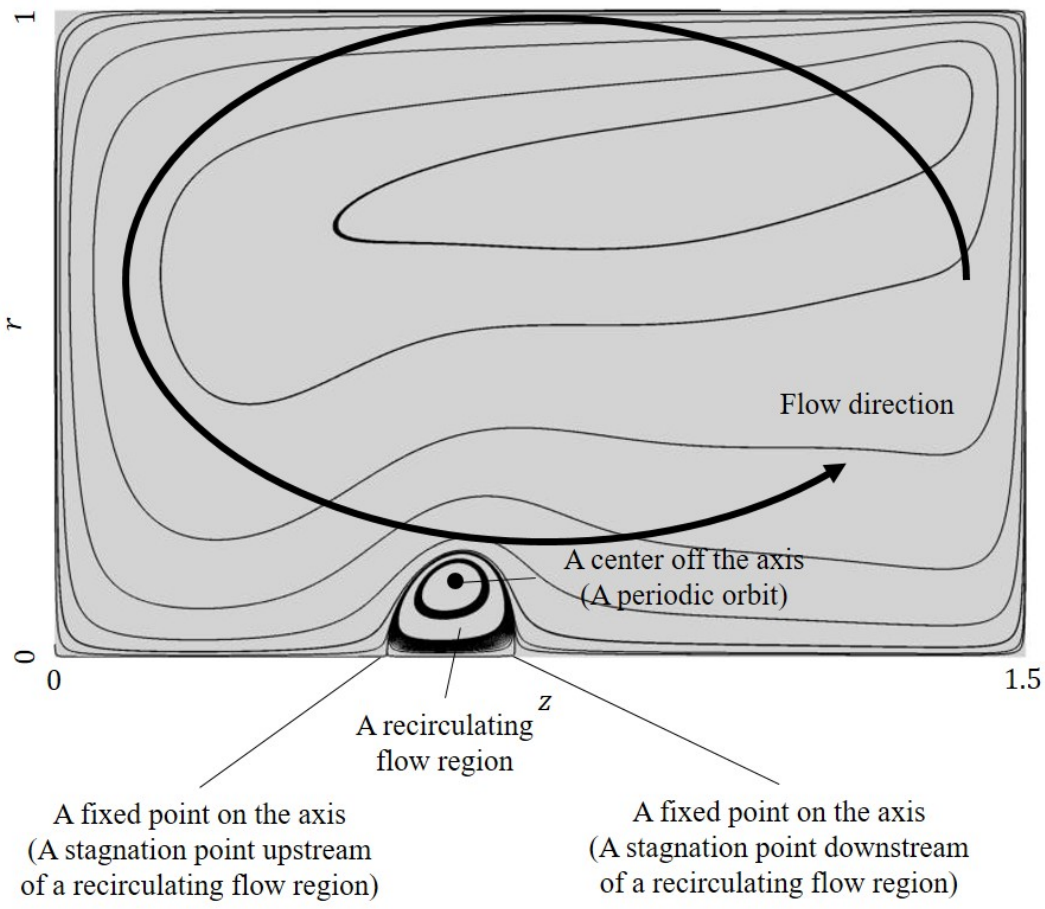

Figure 4.2: Two-dimensional streamlines for $Re = 1256$ in *CC-Incomp* case

respectively. Then, their eigenvalues are

$$\kappa_{up} = 0.062 \pm 0.056i, -0.124, \tag{4.3}$$
$$\kappa_{down} = -0.030 \pm 0.096i, 0.060, \tag{4.4}$$

respectively. We can see all the stagnation point are hyperbolic and the difference is only the sign of the real part of the eigenvalue. Taking the summation of the three eigenvalues, it becomes zero because the numerical solutions well satisfy the solenoidal condition of the velocity vector field for an incompressible flow.

Next, we see how the eigenvalue changes by varying parameters from the onset of the recirculating flow region. Fig. 4.3 shows the change of the eigenvalues for various Reynolds numbers for *CC-Incomp* case. It is shown that, at the onset, there exists only one stagnation point whose velocity gradient tensor is non-hyperbolic:

$$A_{onset} = \begin{pmatrix} 0 & -0.061 & 0 \\ 0.061 & 0 & 0 \\ 0 & 0 & 0 \end{pmatrix}. \tag{4.5}$$

The eigenvalues are

$$\kappa_{onset} = \pm 0.061i, 0. \tag{4.6}$$

4.1.2 Nonlinear bifurcation model

According to Guckenheimer and Holmes [27], we can introduce a two-parameter bifurcation model about this non-hyperbolic fixed point such that

$$\frac{d\check{r}}{dt} = \mu_1 \check{r} + a\check{r}\check{z}, \tag{4.7}$$
$$\frac{d\check{z}}{dt} = \mu_2 + \check{r}^2 + \check{z}^2, \tag{4.8}$$

where μ_1 and μ_2 are bifurcation parameters, and $\check{r}\check{z}$-plane is transformed from rz-plane in order to make the coefficients simple as shown in Chapter 2.. For an axisymmetric incompressible flow, there is only one parameter μ_2 in a bifurcation model of the recirculating flow region by Brøns *et al.* μ_2 is the minimum of the velocity ϖ. If it is negative, the recirculating flow region is observed. However, we need to confirm the second parameter can appear in the context of fluid dynamics, because the mathematics indicates the two-parameter bifurcation. Taking the divergence of the velocity field, we can easily obtain the dilatation such that

$$div(\check{\mathbf{u}}) = 2\mu_1 + 2(a-1)\check{z}. \tag{4.9}$$

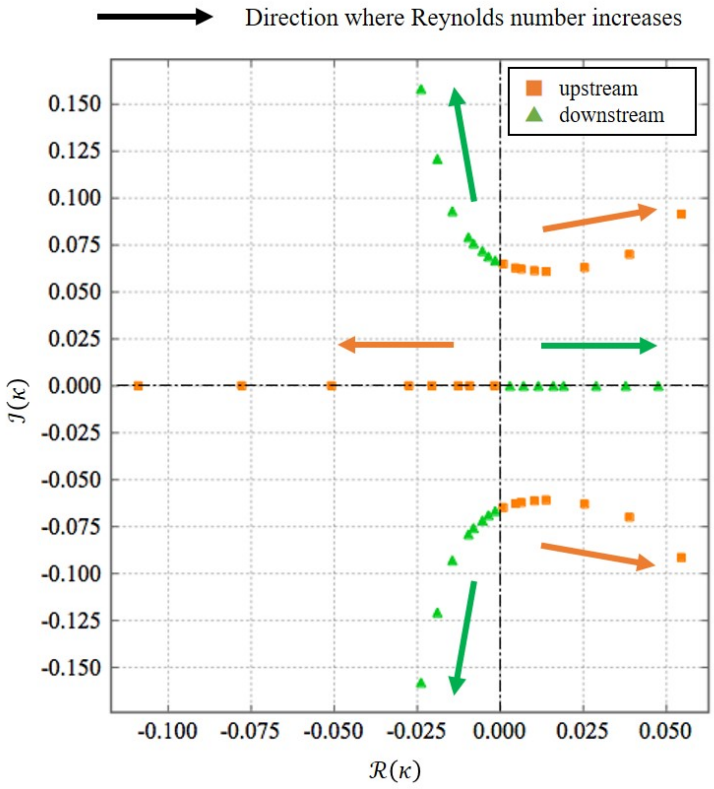

Figure 4.3: Eigenvalues of velocity gradient tensor at stagnation-point pairs for various Reynolds numbers: *arrows indicate the increase in the Reynolds number*

At the same time, we can understand why this second parameter doesn't appear for the incompressible flow. It is because μ_1 must be zero to satisfy the solenoidal condition. Then, it is considered that the other bifurcation by varying μ_1 can be observed in the dynamical system of streamlines. Here, we denote μ_1 by Δ. Also, we rewrite the two-parameter model as

$$\frac{d\check{r}}{dt} = \Delta\check{r} + a\check{r}\check{z}, \tag{4.10}$$

$$\frac{d\check{z}}{dt} = \varpi + \check{r}^2 + \check{z}^2. \tag{4.11}$$

We can conclude that the two-parameter model includes the one-parameter model proposed by Brøns *et al.* [13] and reduces to the one-parameter model when the solenoidal condition is satisfied.

4.2 Axisymmetric low-Mach-number case

(This section is not open to the public, because it will be published as a journal paper.)

4.2.1 Eigenanalysis of velocity gradient tensor

4.2.2 Nonlinear bifurcation model

4.3 Asymmetric case

(This section is not open to the public, because it will be published as a journal paper.)

4.3.1 Eigenanalysis of velocity gradient tensor

4.3.2 Topological structure of streamlines

4.4 Summary of this chapter

(This section is not open to the public, because it will be published as a journal paper.)

Chapter 5

Global Stability Analysis on Bubble-Type Vortex Breakdown

In this chapter, results of stability analyses are shown and discussed. We conduct global stability analyses for direct and adjoint systems based on two types of steady solutions for *SJ-Comp* case. One is axisymmetric and the other is asymmetric. At first, we see results of an axisymmetric case for $(Re, M, \alpha, S, r_{off}) = (200, 0.2, 1.2, 1, 0)$. We check the eigenvalue distribution and then examine both the direct and the adjoint modes. Although there exists previous studies on the same analysis for incompressible flows, the present study can reveal where thermodynamical perturbations grow and originate by the global stablility analysis for a compressible flow. Then, we see where not only motional perturbations but also thermodynamical pertubations grow from the direct mode, while, from the adjoint mode, we see where those pertuabtions originate. Also, we examine the sensitivity indicating where the perturbations are amplified by an internal feedback. It is shown that the sensitivity is high around the stagnation point upstream of the recirculating flow region. Next, we examine the results of asymmetric cases, varying S and r_{off}. Although there is not big difference in the direct and the adjoint modes between the axisymmetric and the asymmetric cases, the highest sensitivity region strongly relates to the place where streamlines just upstream of the recirculating flow region separate to those through and around the recirculating flow region. Fig. 5.1 shows a revised research table by Chapter 4 and what is investigated in Chapter 5.

5.1 Axisymmetric case

(This section is not open to the public, because it is going to be published as a journal paper.)

		Topology	Stability
Incompressible	Axisymmetric	Investigated	Investigated
	Fully three-dimensional	Investigated	Not yet
Compressible	Axisymmetric	Investigated	Not yet
	Fully three-dimensional	Investigated	Not yet

To be investigated in Chapter 5

Figure 5.1: Revised research table by Chapter 4 and what is investigated in Chapter 5

5.1.1 Eigenvalue distibution

5.1.2 Direct and adjoint global modes

5.1.3 Sensitivity

5.2 Asymmetric case

(This section is not open to the public, because it is going to be published as a journal paper.)

5.2.1 Misalignment effect on the least stable eigenvalue

5.2.2 Direct and adjoint global modes

5.2.3 Sensitivity

5.3 Summary of this chapter

(This section is not open to the public, because it will be published as a journal paper.)

Chapter 6

Conclusion

(This chapter is not open to the public, because it is going to be published as a journal paper.)

In this thesis, bubble-type vortex breakdowns were investigated from aspects of its topology and stability. Its aims were to reveal the topology of the bubble-type vortex breakdown for unsteady, fully three-dimensional, and compressible flows, and to reveal the stability, the receptivities, and the sensitivity of the bubble-type vortex breakdown for fully three-dimensional compressible flows.

Results to be analyzed were obtained by a numerical approach. Simulated cases are three cases: an axisymmetric incompressible flow in a closed cylinder (*CC-Incomp*), an axisymmetric low-Mach-number flow in the closed cylinder (*CC-LMN*), and a compressible swirling jet with free-slip boundaryies (*SJ-Comp*). For *SJ-Comp* case, another parameter is added to the classical profile of a longitudinal vortex in order to examine the axisymmetry breaking of a streamline topology.

Finally, Fig. 6.1 shows a revised research table by the present study. Some contents were newly investigated here and we saw there still remains some future works and open problems. We hope those problems will be solved in the near future and the vortex breakdown phenomenon is not only blown out over a delta wing but also utilized in many applications.

		Topology	Stability
Incompressible	Axisymmetric	Investigated	Investigated
	Fully three-dimensional	Investigated	Not yet
Compressible	Axisymmetric	Investigated	Investigated
	Fully three-dimensional	Investigated	Investigated

Figure 6.1: Revised research table by the present study

Acknowlegements

The author really appreciate great guidance of Professor Kojiro Suzuki. Beggining from having told me vortex breakdown and dynamical system theory, he has always let me proceed my research as I wanted and has given me insightful comments when I got stuck. For sure, I would not be what I am now, if I had not been supervised by him. I appriciate my thesis defense examiners, Professor Zensho Yoshida, Professor Kenichi Rinoie, Professor Katsuhiro Nishinari, and Associate Professor Taro Imamura. Their reviewing my dissertation lead me its success.

Through seminars and conferences, I have been luckily endowed with connections to many researchers. I appreciate Dr. Markus Rütten to invite me a research internship at DLR. That was great experience to me. I also appreciate Associate Professor Tsuyoshi Yoneda to give me a chance of collaboration research. I hope to continue collaborating with them in the future.

I would like to thank Assistant Professor Yasumasa Watanabe to kindly help me to deal with any staffs and give appropriate advices many times. I would also like to thank Dr. Yuya Ohmichi to invite me JAXA as a research trainee and tell me state-of-the-art researches and lots of techniques to make an engineering material. I hope to continue collaboration research with him too. I would like to thank Dr. Rei Yamashita to tell me how to precisely express and present my research. I would like to thank Dr. Hisaichi Shibata to be a consult and to often talk with me through his sharp insight. I also acknowledge mates in Ph.D. course to give a lot of fun to me in daily life. Finally, I really thank my parents for tremendous support of my life.

Appendix A

Definition of Inner Product

In this thesis, an inner product $\langle \cdot, \cdot \rangle$ is defined as

$$\langle \mathbf{f}(\mathbf{x}), \mathbf{g}(\mathbf{x}) \rangle = \int_V (f_1(\mathbf{x})g_1(\mathbf{x}) + f_2(\mathbf{x})g_2(\mathbf{x}) + f_3(\mathbf{x})g_3(\mathbf{x}) + f_4(\mathbf{x})g_4(\mathbf{x}) + f_5(\mathbf{x})g_5(\mathbf{x}))dV, \quad \text{(A.1)}$$

where $\mathbf{f} = (f_1, f_2, f_3, f_4, f_5)$ and $\mathbf{g} = (g_1, g_2, g_3, g_4, g_5)$ are state vectors.

From the inner product, we can understand a relation between a direct mode $\mathbf{\Phi}_i$ and an adjoint mode $\mathbf{\Psi}_i$. We can write a solution of perturbation variables as

$$\mathbf{q}'(\mathbf{x}, t) = e^{tL}\mathbf{q}'(\mathbf{x}, 0) = \sum_i e^{\lambda_i t}\langle \mathbf{q}'(\mathbf{x}, \mathbf{0}), \mathbf{\Psi_i} \rangle \mathbf{\Phi_i}. \quad \text{(A.2)}$$

Analyzing eigenvalues and eigenvectors of an original system, we can obtain a temporal growth rate and a corresponding spatial distribution of the perturbation. However, we cannot evaluate the amplitude which indicates an influence of the direct mode on the solution. As shown in the above equation, it is calculated by the inner product of the initial condition and the adjoint mode. It means, when we put a disturbance at a location where the adjoint mode is large, the influence of the direct mode becomes large. It is the reason why the adjoint mode is called a receptivity.

Appendix B

Derivation of Adjoint Navier-Stokes Equations

In researches of optimal designs, there exists *adjoint method*. This method uses adjoint equations to obtain a gradient to an otimized state. Then, we can find adjoint equations for some flow equations in those areas [6]. However, as the adjoint equations for fully three-dimensional compressible Navier-Stoke equations are little investigated, we can find only one example in Otero [45]. Then, the adjoint equations for three-dimensional compressible Navier-Stokes equations are derived here.

We can derive adjoint equations of Eq. 3.53 thorugh an integral by parts using the inner product defined in Appendix A. Applying the integral by parts to $\langle \mathcal{L}\mathbf{q}^{'}, \mathbf{q}^{*} \rangle$, we obtain

$$\langle \mathcal{L}\mathbf{q}^{'}, \mathbf{q}^{*} \rangle = \int_{V} (\mathcal{L}q^{'})_1 q_1^{*} + (\mathcal{L}q^{'})_2 q_2^{*} + (\mathcal{L}q^{'})_3 q_3^{*} + (\mathcal{L}q^{'})_4 q_4^{*} + (\mathcal{L}q^{'})_5 q_5^{*} dV. \tag{B.1}$$

What we want to obtain is

$$\langle \mathbf{q}^{'}, \mathcal{L}^{*}\mathbf{q}^{*} \rangle = \int_{V} q_1^{'}(\mathcal{L}^{*}q^{*})_1 + q_2^{'}(\mathcal{L}^{*}q^{*})_2 + q_3^{'}(\mathcal{L}^{*}q^{*}) + q_4^{'}(\mathcal{L}^{*}q^{*})_4 + q_5^{'}(\mathcal{L}^{*}q^{*})_5 dV. \tag{B.2}$$

Then, we need to precisely integrate the differential terms of $q_i^{'}$ by parts, combine terms into one about $q_i^{'}$, and extract multipliers of $q_i^{'}$. When $\mathcal{L}$ consists of only constants, we need not to integrate this equation by parts. However, linearized Navier-Stokes equations have first-and second-order differential terms, and then, we have to integrate the above equations by parts twice, although we can independently integrate each term.

At first, integrating the linearized continuity equation by parts,

$$\begin{aligned}\int_V (\mathcal{L}q^{'})_1 q_1^* dV &\equiv \int_V -(\partial_x m_x^{'} + \partial_y m_y^{'} + \partial_z m_z^{'})\rho^* dV, \\ &= \int_V m_x^{'}\partial_x\rho^* + m_y^{'}\partial_y\rho^* + m_z^{'}\partial_z\rho^* dV \\ &- \int_{\partial V} (m_x^{'} + m_y^{'} + m_z^{'})\rho^* dA.\end{aligned} \tag{B.3}$$

The integrand of the first term is parts of adjoint equations and the second term is parts of the boundary term, which is required to be zero.

Next, integrating the linearized equation of motion in x-direction by parts,

$$\begin{aligned}\int_V (\mathcal{L}q^{'})_2 q_2^* dV &\equiv \int_V -(\partial_x(m_x^{'}u_x) + \partial_y(m_x^{'}u_y) + \partial_z(m_x^{'}u_z) \\ &\quad +\partial_x(m_x u_x^{'}) + \partial_y(m_x u_y^{'}) + \partial_z(m_x u_z^{'}) \\ &\quad +\partial_x p^{'} - \partial_x\tau_{xx}^{'} - \partial_y\tau_{xy}^{'} - \partial_z\tau_{xz}^{'})m_x^* dV, \\ &= \int_V m_x^{'}u_x\partial_x m_x^* + m_x^{'}u_y\partial_y m_x^* + m_x^{'}u_z\partial_z m_x^* \\ &\quad +m_x u_x^{'}\partial_x m_x^* + m_x u_y^{'}\partial_y m_x^* + m_x u_z^{'}\partial_z m_x^* \\ &\quad +p^{'}\partial_x m_x^* - \tau_{xx}^{'}\partial_x m_x^* - \tau_{xy}^{'}\partial_y m_x^* - \tau_{xz}^{'}\partial_z m_x^* dV \\ &- \int_{\partial V} (m_x^{'}u_x + m_x^{'}u_y + m_x^{'}u_z \\ &\quad m_x u_x^{'} + m_x u_y^{'} + m_x u_z^{'} \\ &\quad p^{'} - \tau_{xx}^{'} - \tau_{xy}^{'} - \tau_{xz}^{'})m_x^* dA.\end{aligned} \tag{B.4}$$

Integrating left derivative terms (viscous shear stress) by parts,

$$\begin{aligned}\int_V -\tau_{xx}^{'}\partial_x m_x^* - \tau_{xy}^{'}\partial_y m_x^* - \tau_{xz}^{'}\partial_z m_x^* dV &= \int_V u_x^{'}(\partial_x\tau_{xx}^* + \partial_y\tau_{xy}^* + \partial_z\tau_{xz}^*)dV \\ &- \int_{\partial V} u_x^{'}(\tau_{xx}^* + \tau_{xy}^* + \tau_{xz}^*)dA.\end{aligned} \tag{B.5}$$

In y-and z-directions,

$$\begin{aligned}
\int_V (\mathcal{L}q^{'})_3 q_3^* dV &\equiv \int_V -(\partial_x(m_y^{'}u_x) + \partial_y(m_y^{'}u_y) + \partial_z(m_y^{'}u_z) \\
&\quad +\partial_x(m_y u_x^{'}) + \partial_y(m_y u_y^{'}) + \partial_z(m_y u_z^{'}) \\
&\quad +\partial_y p^{'} - \partial_x \tau_{yx}^{'} - \partial_y \tau_{yy}^{'} - \partial_z \tau_{yz}^{'}) m_y^* dV, \\
&= \int_V m_y^{'} u_x \partial_x m_y^* + m_y^{'} u_y \partial_y m_y^* + m_y^{'} u_z \partial_z m_y^* \\
&\quad +m_y u_x^{'} \partial_x m_y^* + m_y u_y^{'} \partial_y m_y^* + m_y u_z^{'} \partial_z m_y^* \\
&\quad +p^{'} \partial_y m_y^* - \tau_{yx}^{'} \partial_x m_y^* - \tau_{yy}^{'} \partial_y m_y^* - \tau_{yz}^{'} \partial_z m_y^* dV \\
&- \int_{\partial V} (m_y^{'} u_x + m_y^{'} u_y + m_y^{'} u_z \\
&\quad m_y u_x^{'} + m_y u_y^{'} + m_y u_z^{'} \\
&\quad p^{'} - \tau_{yx}^{'} - \tau_{yy}^{'} - \tau_{yz}^{'}) m_y^* dA,
\end{aligned} \tag{B.6}$$

$$\begin{aligned}
\int_V (\mathcal{L}q^{'})_4 q_4^* dV &\equiv \int_V -(\partial_x(m_z^{'}u_x) + \partial_y(m_z^{'}u_y) + \partial_z(m_z^{'}u_z) \\
&\quad +\partial_x(m_z u_x^{'}) + \partial_y(m_z u_y^{'}) + \partial_z(m_z u_z^{'}) \\
&\quad +\partial_z p^{'} - \partial_x \tau_{zx}^{'} - \partial_y \tau_{zy}^{'} - \partial_z \tau_{zz}^{'}) m_z^* dV, \\
&= \int_V m_z^{'} u_x \partial_x m_z^* + m_z^{'} u_y \partial_y m_z^* + m_z^{'} u_z \partial_z m_z^* \\
&\quad +m_z u_x^{'} \partial_x m_z^* + m_z u_y^{'} \partial_y m_z^* + m_z u_z^{'} \partial_z m_z^* \\
&\quad +p^{'} \partial_x m_z^* - \tau_{zx}^{'} \partial_x m_z^* - \tau_{zy}^{'} \partial_y m_z^* - \tau_{zz}^{'} \partial_z m_z^* dV \\
&- \int_{\partial V} (m_z^{'} u_x + m_z^{'} u_y + m_z^{'} u_z \\
&\quad m_z u_x^{'} + m_z u_y^{'} + m_z u_z^{'} \\
&\quad p^{'} - \tau_{zx}^{'} - \tau_{zy}^{'} - \tau_{zz}^{'}) m_z^* dA,
\end{aligned} \tag{B.7}$$

respectively. Integrating left derivative terms (viscous shear stress) by parts,

$$\begin{aligned}\int_V -\tau_{yx}^{'}\partial_x m_y^* - \tau_{yy}^{'}\partial_y m_y^* - \tau_{yz}^{'}\partial_z m_y^* dV &= \int_V u_y^{'}(\partial_x\tau_{yx}^* + \partial_y\tau_{yy}^* + \partial_z\tau_{yz}^*)dV \\ &- \int_{\partial V} u_y^{'}(\tau_{yx}^* + \tau_{yy}^* + \tau_{yz}^*)dA, \end{aligned} \tag{B.8}$$

$$\begin{aligned}\int_V -\tau_{zx}^{'}\partial_x m_z^* - \tau_{zy}^{'}\partial_y m_z^* - \tau_{zz}^{'}\partial_z m_z^* dV &= \int_V u_z^{'}(\partial_x\tau_{zx}^* + \partial_y\tau_{zy}^* + \partial_z\tau_{zz}^*)dV \\ &- \int_{\partial V} u_z^{'}(\tau_{zx}^* + \tau_{zy}^* + \tau_{zz}^*)dA., \end{aligned} \tag{B.9}$$

respectively.

At last, integrating the linearized pressure equation by parts,

$$\begin{aligned}\int_V (\mathcal{L}q^{'})_5 q_5^* dV &\equiv \int_V \{-[\partial_x(p^{'}u_x) + \partial_y(p^{'}u_y) + \partial_z(p^{'}u_z) + \partial_x(pu_x^{'}) + \partial_y(pu_y^{'}) + \partial_z(pu_z^{'})] \\ &+(\gamma-1)[-p'(\partial_x u_x + \partial_y u_y + \partial_z u_z) - p(\partial_x u_x^{'} + \partial_y u_y^{'} + \partial_z u_z^{'}) + \partial_x q_x^{'} + \partial_y q_y^{'} + \partial_z q_z^{'} \\ &+\partial_x u_x^{'}\tau_{xx} + \partial_y u_y^{'}\tau_{yy} + \partial_z u_z^{'}\tau_{zz} + \partial_x u_x\tau_{xx}^{'} + \partial_y u_y\tau_{yy}^{'} + \partial_z u_z\tau_{zz}^{'} \\ &+(\partial_x u_y^{'} + \partial_y u_x^{'})\tau_{xy} + (\partial_y u_z^{'} + \partial_z u_y^{'})\tau_{yz} + (\partial_z u_x^{'} + \partial_x u_z^{'})\tau_{zx} \\ &+(\partial_x u_y + \partial_y u_x)\tau_{xy}^{'} + (\partial_y u_z + \partial_z u_y)\tau_{yz}^{'} + (\partial_z u_x + \partial_x u_z)\tau_{zx}^{'}]\}p^* dV, \\ &= \int_V p^{'}u_x\partial_x p^* + p^{'}u_y\partial_y p^* + p^{'}u_z\partial_z p^* + pu_x^{'}\partial_x p^* + pu_y^{'}\partial_y p^* + pu_z^{'}\partial_z p^* \\ &-(\gamma-1)[p'p^*(\partial_x u_x + \partial_y u_y + \partial_z u_z) - u_x^{'}\partial_x(pp^*) - u_y^{'}\partial_y(pp^*) - u_z^{'}\partial_z(pp^*) \\ &+q_x^{'}\partial_x p^* + q_y^{'}\partial_y p^* + q_z^{'}\partial_z p^* \\ &+u_x^{'}\tau_{xx}\partial_x p^* + u_y^{'}\tau_{yy}\partial_y p^* + u_z^{'}\tau_{zz}\partial_z p^* + \partial_x u_x M_{xx} + \partial_y u_y M_{yy} + \partial_z u_z M_{zz} \\ &+(u_y^{'}\partial_x p^* + u_x^{'}\partial_y p^*)\tau_{xy} + (u_z^{'}\partial_y p^* + u_y^{'}\partial_z p^*)\tau_{yz} + (u_x^{'}\partial_z p^* + u_z^{'}\partial_x p^*)\tau_{zx} \\ &+(\partial_x u_y + \partial_y u_x)M_{xy} + (\partial_y u_z + \partial_z u_y)M_{yz} + (\partial_z u_x + \partial_x u_z)M_{zx}]dV \\ &- \int_{\partial V}\{-(p^{'}u_x + p^{'}u_y + p^{'}u_z + pu_x^{'} + pu_y^{'} + pu_z^{'}) \\ &+(\gamma-1)[-p(u_x^{'} + u_y^{'} + u_z^{'}) + q_x^{'} + q_y^{'} + q_z^{'} \\ &+u_x^{'}\tau_{xx} + u_y^{'}\tau_{yy} + u_z^{'}\tau_{zz} + (u_y^{'} + u_x^{'})\tau_{xy} + (u_z^{'} + u_y^{'})\tau_{yz} + (u_x^{'} + u_z^{'})\tau_{zx}]\}p^* dA, \end{aligned} \tag{B.10}$$

where

$$M_{ij} \equiv \mu(u_i^{'}\partial_j p^* + u_j^{'}\partial_i p^* - \frac{2}{3}u_k^{'}\partial_k p^*) - \frac{d\mu}{dT}\frac{\tau_{ij}}{\mu}T'p^*. \tag{B.11}$$

Integrating left terms by parts,

$$\begin{aligned} & \int_V -(\gamma-1)(q_x^{'}\partial_x p^* + q_y^{'}\partial_y p^* + q_z^{'}\partial_z p^*)dV \qquad \text{(B.12)} \\ = & \int_V \frac{\mu}{RePrM^2}T^{'}(\partial_x^2 p^* + \partial_y^2 p^* + q_z^{'}\partial_z p^*)dV \\ - & \int_{\partial V} \frac{\mu}{RePrM^2}T^{'}(\partial_x p^* + \partial_y p^* + \partial_z p^*)dA. \end{aligned}$$

Combining above terms about each adjoint variable, we can obtain the adjoint equation shown in Chapter 3. Also, taking the summation of the integrals around boundaries, we can obtain the boundary term.

Appendix C

Validation of numerical differences between direct and adjoint eigensystems

(This chapter is not open to the public, because it is going to be published as a journal paper.)

Appendix D

Effect of Mach Number on Unstable Mode

(This chapter is not open to the public, because it is going to be published as a journal paper.)

Bibliography

[1] E. Åkervik, L. Brandt, D. S. Henningson, J. Hoepffner, and P. Schiatter. Steady solutions of the navier-stokes equations by selective frequency damping. *Physics of Fluids*, 18:068102–1–068102–4, 2006.

[2] W. E. Arnoldi. The principle of minimized interations in the solution of the matrix eigenvalue problem. *Quartery of Applied Mechanics*, 9:17–29, 1951.

[3] G. K. Batchelor and A. E. Gill. Analysis of the stability of axisymmetric jets. *Jouranal of Fluid Mechanics*, 14:529–551, 1962.

[4] B. Benjamin. Theory of vortex breakdown phenomenon. *Journal of Fluid Mechanics*, 14:593–629, 1962.

[5] B. Benjamin. Some developments in the theory of vortex breakdown. *Journal of Fluid Mechanics*, 28:65–84, 1967.

[6] T. R. Bewley, P. Moin, and R. Temam. Dns-based predictive control of turbulence: an optimal benchmark for feedback algorithms. *Journal of Fluid Mechanics*, 447:179–225, 2001.

[7] A. V. Bisgaard, M. Brøns, and J. N. Sørensen. Vortex breakdown generated by off-axis bifurcation in a cylinder with rotating covers. *Acta Mechanica*, 187:75–83, 2006.

[8] D. Blackmore. Simple dynamical models for vortex breakdown of the b-type. *Acta Mechanica*, 102:91–101, 1994.

[9] M. Breuer, D. Hänel, J. Klöker, and M. Meinke. Computation of unsteady vortical flows. *Computer and Fluids*, 22:229–237, 1993.

[10] M. Brøns and J. N. Hartnack. Streamline topologies near simple degenerate critical points in two-dimensional flow away from boundaries. *Physics of Fluids*, 11:314–324, 1999.

[11] M. Brøns, W. Z. Shen, J. N. Sørensen, and W. J. Zhu. The influence of imperfections on the flow structure of steady vortex breakdown bubbles. *Jounal of Fluid Mechanics*, 578:453–466, 2007.

[12] M. Brøns, M. C. Thompson, and K. Hourigan. Dye visualization near a three-dimensional stagnation point: application to the vortex breakdown bubble. *Jounal of Fluid Mechanics*, 622:177–194, 2009.

[13] M. Brøns, L. K. Voigt, and J. N. Sørensen. Streamline topology of steady axisymmetric vortex breakdown in a cylinder with co- and counter-rotating end-covers. *Jounal of Fluid Mechanics*, 401:275–292, 1999.

[14] J. M. Chomaz. Global instabilities in spatially developing flows: non-normality and nonlinearity. *Annual Review of Fluid Mechanics*, 37:357–392, 2005.

[15] M. S. Chong, A. E. Perry, and B. J. Cantwell. A general classification of three-dimensional flow fields. *Physics of Fluids*, 2(5):765–777, 1990.

[16] A. J. Chorin. A numerical method for solving incompressible viscous flow problems. *Journal of Computational Physics*, 2(1):12–26, 1967.

[17] U. C. Dallmann. *Zur identifikation und beschreibung räumlicher strömungsstrukturen und stromungsstrukturänderungen*. PhD thesis, University of Göttingen, 1995.

[18] L. E. Eriksson and A. Rizzi. Computer-aided analysis of the convergence to steady state of discrete approximation to the euler equations. *Journal of Computational Physics*, 57:90–128, 1985.

[19] M. P. Escudier. Observations of the flow produced in a cylindrical container by a rotating endwall. *Experiments in Fluids*, 2(4):189–196, 1984.

[20] F. Feudel, A. Witt, M. Gellert, J. Kurths, C. Grebogi, and M. A. F. Sanjuán. Intersections of stable and unstable manifolds: the skelton of lagrangian chaos. *Chaos, Solitons and Fractrals*, 24:947–956, 2005.

[21] F.Gallaire, M. Ruith, E. Meiburg, J.-M. Chomaz, and P. Huerre. Spiral vortex breakdown as a global mode. *Jounal of Fluid Mechanics*, 549:71–80, 2006.

[22] F.Giannetti and P. Luchini. Structural sensitivity of the first instability of the cylinder wake. *Jounal of Fluid Mechanics*, 581:167–197, 2007.

[23] M. Furukawa, M. Inoue, K. Saiki, and K. Yamada. The role of tip leakage vortex breakdown in compressor rotor aerodynamics. *Journal of Turbomachinery*, 121(3):469–480, 1999.

[24] F. Giannetti and P. Luchini. Receptivity of the circular cylinder's first instability. In *Proceedings of 5th European Fluid Mechanics Conference*, 2003.

[25] M. Giles and N. Pierce. Adjoint equations in cfd - duality, boundary conditions and solution behaviour. In *13th Computational Fluid Dynamics Conference*, 1997.

[26] W. G. Grabowski and S. A. Berger. Solutions of the navier-stokes equations for vortex breakdown. *Jounal of Fluid Mechanics*, 75:525–544, 1976.

[27] J. Guckenheimer and P. Holmes. *Nonlinear Oscillations, Dynamical Systems, and Bifurcations of Vetor Fields*. Springer, 1983.

[28] M. G. Hall. Vortex breakdown. *Annual Review of Fluid Mechanics*, 4:195–218, 1972.

[29] M. G. Harvey. Some observations of the vortex breakdown phenomenon. *Annual Review of Fluid Mechanics*, 14:585–592, 1962.

[30] T. Herbert. Parabolized stability equations. *Annual Review of Fluid Mechanics*, 29:245–283, 1997.

[31] P. Holmes. Some remarks on chaotic particle paths in time-periodic, three-dimensional swirling flows. *Contemporary Mathematics*, 28:393–404, 1984.

[32] P. Huerre and P. A. Monkewitz. Local and global instabilities in spatially developing flows. *Annual Review of Fluid Mechanics*, 22:473–537, 1990.

[33] T. Kajishima and K. Taira. *Computational Fluid Dynamics Incompressible Turbulent Flows*. Springer, 2017.

[34] A. N. Krylov. On the numerical solution of the equations by which in technical questions frequencies of small oscillations of material systems are determined. *Izvestija AN USSR (News of Acadamy of Sciences of the USSR)*, 7(4):491–539, 1931.

[35] A. Lankadasu and S. Vengadesan. Onset of vortex shedding in planar shear flow past a square cylinder. *Jounal of Heat and Fluid Flow*, 29:1054–1059, 2008.

[36] S. K. Lele. Compact finite difference schemes with spectral-like resolution. *Jounal of Computational Physics*, 103:16–42, 1992.

[37] J. M. Lopez. Axisymmetric vortex breakdown. part 1 confined swirling flow. *Jounal of Fluid Mechanics*, 221:533–552, 1990.

[38] J. M. Lopez and A. D. Perry. Axisymmetric vortex breakdown. part 3 onset of periodic flow and chaotic advection. *Jounal of Fluid Mechanics*, 234:449–471, 1992.

[39] E. N. Lorenz. Deterministic nonperiodic flow. *Jounal of Atmospheric Science*, 20:130–141, 1963.

[40] A. Majda and J. Sethian. The derivation and numerical solution of the equations for zero mach number combustion. *Combustion Science and Technology*, 42:185–205, 1985.

[41] O. Marquet, D. Sipp, and L. Jacquin. Sensitivity analysis and passive control of cylinder flow. *Journal of Fluid Mechanics*, 615:221–252, 2008.

[42] P. Meliga and F. Gallaire. Control of axisymmetric vortex breakdown in a constricted pipe: Nonlinear steady states and weakly nonlinear asymptotic expansions. *Physics of Fluids*, 23:84–102, 2011.

[43] F. Nicoud. Conservative high-order finitie-difference schemes for low-mach number flows. *Journal of Computational Physics*, 158:71–97, 2000.

[44] S. A. Orszag. Accurate solution of the orr-sommerfeld stability equation. *Journal of Fluid Mechanics*, 50:689–703, 1971.

[45] J. Otero. *Development and application of an adjoint-based optimal flow control framework for compressible direct numerical simulations*. PhD thesis, University of Southampton, 2017.

[46] D. H. Peckham and S. A. Atkinson. Preliminary results of low speed wind tunnel tests on a gothic wing of aspect ratio 1.0. In *Aeronautical Research Council*, 1957.

[47] A. E. Perry and M. S. Chong. A description of eddying motionsand flow patterns using critical-point concepts. *Annual Review of Fluid Mechanics*, 19:125–155, 1987.

[48] T. J. Poinsot and S. K. Lele. Boundary conditions for direct simulations of compressible viscous flows. *Journal of Computational Physics*, 101:104–129, 1992.

[49] U. A. Qadri, D. Mistry, and M. P. Juniper. Structural sensitivity of spiral vortex breakdown. *Journal of Fluid Mechanics*, 720:558–581, 2013.

[50] O. Reynolds. An experimental investigation of the circumstances which determine whether the motion of water shall be direct or sinuous, and of the law of resistance in parallel channels. *Proceedings of the Royal Society London*, 35:84–99, 1883.

[51] R. Rottuno. The fluid dynamics of tornadoes. *Annual Review of Fluid Mechanics*, 45:59–84, 2013.

[52] M. R. Ruith, P. Chen, E. Meiburg, and T. Maxworthy. Three-dimensional vortex breakdown in swirling jets and wakes. *Journal of Fluid Mechanics*, 486:331–378, 2003.

[53] Y. Saad. Variations on arnoldi's method for computing eigenelements of large unsymmetric matrices. *Linear Algebra and its Applications*, 34:269–295, 1980.

[54] T. Sarpkaya. On stationary and travelling vortex breakdowns. *Journal of Fluid Mechanics*, 45:545–559, 1971.

[55] T. Sarpkaya. Turbulent vortex breakdown. *Physics of Fluids*, 7(10):2301–2303, 1995.

[56] L. P. Shilnikov. A case of the existence of a denumerable set of periodic motions. *Soviet Mathematics Doklady*, 6:163–166, 1965.

[57] F. Sotilopoulos and Y. Ventikos. The three-dimensional structure of confined swirling flows with vortex breakdown. *Jounal of Fluid Mechanics*, 426:155–175, 2001.

[58] F. Sotilopoulos, Y. Ventikos, and T. C. Lackey. Chaotic advection in three-dimensional stationary vortex-breakdown bubbles: Šil'nikov's chaos and devil's staircase. *Jounal of Fluid Mechanics*, 444:257–297, 2001.

[59] R. E. Spall and T. B. Gatski. Numerical calculations of three-dimensional turbulent vortex breakdown. *International Journal for Numerical Methods in Fluids*, 20:307–318, 1995.

[60] N. Syred. A review of oscillation mechanisms and the role of the precessing vortex core (pvc) in swirl combustion systems. *Progress in Energy and Combustion Science*, 32:93–161, 2006.

[61] K. W. Thompson. Time development boundary conditions for hyperbolic systems. *Journal of Computational Physics*, 68:1–24, 1987.

[62] G. A. Thouas, J. Sheridan, and K. Hourigan. A bioreactor model of mouse tumor progression. *Journal of Biomedicine and Biotechnology*, 2007:1–9, 2007.

[63] M. Tobak and D. J. Peake. Topology of three-dimensional separated flows. *Annual Review of Fluid Mechanics*, 14:61–85, 1982.

[64] G. S. Triantayllou, M. S. Triantayllou, and C. Chryssostomidis. On the formation of vortex sheets behind stationary cylinders. *Journal of Fluid Mechanics*, 170:461–477, 1986.

[65] D. J. Tritton. *Physical fluid dynamics*. Springer, 1977.

[66] M. R. Visbal. Computational and physical aspects of vortex brekdown on delta wings. In *33rd Aerospace and Science Meeting and Exhibit*, 1995.

[67] H. U. Vogel. *Experimentelle ergebnisse über die laminare strömung in einem zylindrischen gehäuse mit darin rotierender scheibe*. PhD thesis, MPI Strömungsforschung, 1968.

[68] S. Wang and Z. Rusak. The dynamics of a swirling flow in a pipe and transition to axisymmetric vortex breakdown. *Journal of Fluid Mechanics*, 340:177–223, 1997.

[69] S. Wiggins. *Introduction to Applied Nonlinear Dynamical Systems and Chaos*. Springer, 1990. (Translated into Japanese by T. Niwa in 1992).

[70] C. H. K. Williamson. Vortex dynamics in the cylinder wake. *Annual Review of Fluid Mechanics*, 28:477–539, 1996.

[71] G. B. Willis. *One-Dimensional two-phase flow*. McGraw Hill, 1969.

[72] K. Yamada and K. Suzuki. Dynamical system analysis on the onset of recirculating flow region associated with vortex breakdown. In *46th AIAA Fluid Dynamics Conference*, 2016.

[73] S. Zhang, H. Zhang, and C.-W. Shu. Topological structure of shock induced vortex breakdown. *Journal of Fluid Mechanics*, 639:343–372, 2009.

List of Publication and Presentation

Publication

- K. Yamada and K. Suzuki. Numerical study on detailed structure of vortex breakdown behaviour for Landing spaceplane. *Transactions of the Japan Society for Aeronautical and Space Sciences, Aerospace Technology Japan,* ists30:Pe_77-Pe_85, 2016.

Presentation

- K. Yamada and K. Suzuki. Compressiblity effect on topology of vortex ring formed by vortex breakdown in closed cylinder at low-Mach-numbers. *8th AIAA Theoretcal Fluid Mechanics Conference,* Denver, CO, 2017.
- K. Yamada and K. Suzuki. Dynamical system analysis on the onset of recirculating flow region associated with vortex breakdown. *46th AIAA Fluid Dynamics Conference,* Washington, DC, 2016.